

A generalised, multi-phase-field theory for dissolution-driven stress corrosion cracking and hydrogen embrittlement

Chuanjie Cui^{a,b}, Rujin Ma^{b,c}, Emilio Martínez-Pañeda^{a,*}

^a*Department of Civil and Environmental Engineering, Imperial College London, London SW7 2AZ, UK*

^b*College of Civil Engineering, Tongji University, Shanghai 200092, China*

^c*Key Laboratory of Performance Evolution and Control for Engineering Structures, Tongji University, Shanghai 200092, China*

Abstract

We present a phase field-based electro-chemo-mechanical formulation for modelling mechanics-enhanced corrosion and hydrogen-assisted cracking in elastic-plastic solids. A multi-phase-field approach is used to present, for the first time, a general framework for stress corrosion cracking, incorporating both anodic dissolution and hydrogen embrittlement mechanisms. We numerically implement our theory using the finite element method and defining as primary kinematic variables the displacement components, the phase field corrosion order parameter, the metal ion concentration, the phase field fracture order parameter and the hydrogen concentration. Representative case studies are addressed to showcase the predictive capabilities of the model in various materials and environments, attaining a promising agreement with benchmark tests and experimental observations. We show that the generalised formulation presented can capture, as a function of the environment, the interplay between anodic dissolution- and hydrogen-driven failure mechanisms; including the transition from one to the other, their synergistic action and their individual occurrence. Such a generalised framework can bring new insight into environment-material interactions and the understanding of stress corrosion cracking, as demonstrated here by providing the first simulation results for Gruhl's seminal experiments.

Keywords: Multi-phase-field, Stress corrosion cracking, Anodic dissolution, Hydrogen embrittlement, Fracture mechanics

*Corresponding author.

Email address: e.martinez-paneda@imperial.ac.uk (Emilio Martínez-Pañeda)

Contents

1	Introduction	3
2	Theory	5
2.1	Kinematics and primal fields	6
2.2	Principle of virtual work and force balances	8
2.3	Energy imbalance	10
2.4	Free energy density	10
2.4.1	Mechanical free energy density	10
2.4.2	Electrochemical energy density	11
2.4.3	Dissolution interface energy density	12
2.4.4	Fracture interface energy density	12
2.4.5	Hydrogen-chemical energy density	13
2.5	Constitutive theory	13
2.5.1	Chemo-elastoplasticity	15
2.5.2	A phase field description of metallic corrosion	15
2.5.3	Transport of ionic species	17
2.5.4	A phase field description of fracture	18
2.5.5	Diffusion of atomic hydrogen	18
2.6	Summary of the governing equations	19
2.6.1	Strong form and multi-physics interactions	19
2.6.2	A brief discussion on ℓ_d and ℓ_f	20
3	Numerical implementation	21
3.1	Weak form	21
3.2	Finite element discretisation	22
3.3	Residuals and stiffness matrices	23
4	Results	24
4.1	Growth of a semi-circular pit	24
4.2	Hydrogen assisted cracking of a notched square plate	28
4.3	Bending of stainless steel samples: transition from anodic dissolution to hydrogen embrittlement	31
4.4	SCC threshold predictions in artificial and biologically-active seawater	36
4.5	SCC tube testing of Al alloys (Gruhl, 1984): hydrogen embrittlement vs anodic dissolution . . .	43
5	Discussion and summary	49

1. Introduction

Predicting the failure of engineering components in aggressive environments is a longstanding scientific challenge with important technological implications (Turnbull, 1993; Martínez-Pañeda, 2021). The combination of mechanical load and corrosive environments facilitates the nucleation and growth of cracks, in what is commonly referred to as *stress corrosion cracking* (SCC). The term stress corrosion cracking broadly encapsulates a wide range of mechanisms. These include local metallic dissolution, rupture of the protective passive film, and uptake of pernicious species such as hydrogen, which can be generated as a result of cathodic reactions in acid environments or through hydrolysis reactions during the corrosion process (Raja and Shoji, 2011). SCC phenomena can be generally classified into two categories. The first one refers to fracture events driven by local material dissolution at the crack tip, as a result of anodic corrosion reactions (Scully, 1975, 1980; Ford, 1990; MacDonald and Urquidi-MacDonald, 1991). The second one is governed by the uptake and diffusion of hydrogen within the crystal lattice, resulting in embrittlement (Gangloff, 2003; Barrera et al., 2018; Djukic et al., 2019). These two classes of phenomena have been investigated extensively, but independently from each other. Examples of anodic-driven models include the surface mobility model (Galvele, 1987), anodic reaction-induced cleavage (Sieradzki and Newman, 1985) and slip-dissolution (Andresen and Ford, 1988; Parkins, 1996; Engelhardt et al., 1999); while hydrogen assisted cracking has been rationalised through decohesion-based mechanisms (Gerberich et al., 1991; Martínez-Pañeda et al., 2016b), hydrogen-dislocation interactions (Sofronis and Birnbaum, 1995; Lynch, 2019) and cleavage driven by hydride formation (Lufrano et al., 1998; Shishvan et al., 2020). However, anodic- and hydrogen-driven SCC phenomena often act in concert and, as a result, there is a need for a generalised theory that can encapsulate their interaction and synergistic effects.

The various hydrogen and dissolution mechanisms involved in SCC are strongly coupled and encompass various physical phenomena. For example, the presence of a passivation film prevents hydrogen ingress in the metal but the film can be ruptured by crack tip straining. Also, pits resulting from localised material dissolution will facilitate hydrogen uptake by changing the local electrolyte pH and by acting as stress concentrators, as hydrogen accumulates in areas of high hydrostatic stress. The need for capturing multiple chemical and mechanical phenomena, and

their interplay, is arguably one of the reasons why predicting SCC is considered a longstanding challenge (Turnbull, 2001; Jivkov, 2004). Another important challenge is the interfacial nature of SCC. The shape of the SCC defect plays a significant role in the electrolyte chemistry, the nearby mechanical fields and the hydrogen uptake; in turn, these factors govern local corrosion kinetics and thus the morphology of the aqueous electrolyte-solid metal interface. Resolving the underlying processes requires tracking the evolution of the corrosion front, a well-known computational challenge (Duddu et al., 2016; Dekker et al., 2021; Chen et al., 2021). Phase field methods have emerged as a compelling approach for modelling coupled interfacial problems. Evolving interfaces can readily be simulated by using an auxiliary *phase field* variable that takes a distinct value in each of the phases (e.g., 0 and 1) and varies smoothly in-between. The interface then evolves based on the solution to the phase field differential equation, a diffuse interface description that brings multiple advantages: (i) it requires no special treatment or presumptions, as the interface equation is solved in the entire domain; (ii) it can readily handle topological changes such as division or merging of interfaces; and (iii) it can be easily combined with equations describing various physical phenomena. The phase field paradigm has been recently extended to model hydrogen embrittlement (Martínez-Pañeda et al., 2018; Wu et al., 2020; Kristensen et al., 2020b) and material dissolution (Mai et al., 2016; Nguyen et al., 2018; Cui et al., 2021; Ansari et al., 2021; Lin and Ruan, 2021). However, a generalised model encompassing these two key elements of SCC, and their interactions, has not been presented yet.

In this work, we present a generalised formulation for dissolution-driven SCC and hydrogen embrittlement. A multi-phase field paradigm is used to capture interface evolution due to both short range corrosion reactions and mechanical crack growth, including their synergistic interaction. By simulating the evolving morphology of the electrolyte-metal interface, the underlying physical mechanisms can be resolved and the role of SCC defects (pits, cracks) can be investigated. The diffusion of metal ions away from the interface is also modelled to capture the interplay between diffusion- and activation-controlled corrosion. Moreover, we incorporate the role of passivation and the rupture of the passive film upon attaining a critical strain rate (Parkins, 1987; Cui et al., 2021). The transport of hydrogen within the crystal lattice is predicted by means of an extended version of Fick’s law and the impact of hydrogen content on the material toughness is accounted for by means of a quantum-mechanical approach (Serebrinsky et al.,

2004; Martínez-Pañeda et al., 2018). Mechanical deformation is modelled using J_2 flow theory and we incorporate the role of mechanical fields in enhancing corrosion kinetics (Gutman, 1998) and bulk hydrogen diffusion (Sofronis and McMeeking, 1989; Martínez-Pañeda et al., 2016a). We numerically implement our generalised theory using the finite element method and demonstrate its predictive capabilities by analysing several representative case studies. First, two representative benchmarks are addressed to validate the pitting corrosion and hydrogen embrittlement predictive capabilities of the model. Then, numerical experiments are conducted to compare, qualitatively and quantitatively, model predictions against testing data and observations. A wide range of environments are considered, spanning the transition from hydrogen-driven to dissolution-assisted SCC. The competition and interplay between these two phenomena are investigated by: (i) simulating the failure of stainless steel samples under bending, (ii) predicting SCC thresholds in artificial and biologically-active seawater, and (iii) modelling the seminal experiments by Gruhl (1984) on an AlZn5Mg3 alloy. A good agreement with experimental observations is attained.

Notation. We use lightface italic letters for scalars, e.g. ϕ , upright bold letters for vectors, e.g. \mathbf{u} , and bold italic letters, such as $\boldsymbol{\sigma}$, for second and higher order tensors. First-, second-, and fourth-order tensors are in most cases respectively represented by small Latin, small Greek, and capital Latin letters. Inner products are denoted by a number of vertically stacked dots, corresponding to the number of indices over which summation takes place, such that $\boldsymbol{\sigma} : \boldsymbol{\varepsilon} = \sigma_{ij} \varepsilon_{ij}$, with indices referring to a Cartesian coordinate system. The gradient and the Laplacian are respectively denoted by $\nabla \mathbf{u} = u_{i,j}$ and $\nabla^2 \phi = \phi_{,ii}$. Finally, divergence is denoted by $\nabla \cdot \boldsymbol{\sigma} = \sigma_{ij,j}$, the trace of a second order tensor is written as $\text{tr } \boldsymbol{\varepsilon} = \varepsilon_{ii}$, and the deviatoric part of a tensor is given by $\boldsymbol{\sigma}' = \sigma_{ij} - \delta_{ij} \sigma_{kk}$, with δ_{ij} denoting the Kronecker delta.

2. Theory

In this Section we formulate our generalised multi-phase-field theory, aimed at predicting the evolution of the aqueous electrolyte-solid metal interface due to corrosion, embrittlement and fracture processes. The theory refers to the electro-chemo-mechanical response of a domain $\Omega \subset \mathbb{R}^n$ ($n \in [1, 2, 3]$) with external boundary $\partial\Omega \subset \mathbb{R}^{n-1}$, on which the outwards unit normal is denoted as \mathbf{n} . For simplicity, isothermal conditions and isotropic material behaviour are

2.1. Kinematics and primal fields

The figure illustrates a corrosion problem using a phase field model. The main diagram shows a cross-section of a metal structure with a passive film, aqueous electrolyte, and plastic zone. The metal is represented by a gray region, the passive film by a light blue region, and the aqueous electrolyte by a darker blue region. The plastic zone is indicated by a brownish area. Various boundary conditions and physical parameters are labeled, including chemical potentials, concentrations, and mechanical forces. An inset shows the phase field definition with a sharp interface, plotting the phase field ϕ against position x , with regions for ϕ_d and ϕ_f .

Regarding the displacement field \mathbf{u} , the outer surface of the body can be decomposed into a part $\partial\Omega_u$, where the displacement is prescribed by Dirichlet-type boundary conditions, and a part $\partial\Omega_T$, where a traction \mathbf{T} is prescribed by Neumann-type boundary conditions. Also, small

strains are assumed, such that the total strain tensor $\boldsymbol{\varepsilon}$ reads

$$\boldsymbol{\varepsilon} = \frac{1}{2} (\nabla \mathbf{u}^T + \nabla \mathbf{u}) . \quad (1)$$

And the standard decomposition of strains into elastic and plastic components is adopted, such that:

$$\boldsymbol{\varepsilon} = \boldsymbol{\varepsilon}^e + \boldsymbol{\varepsilon}^p . \quad (2)$$

Regarding the transport of ionic or atomic species, the external surface consists of two parts: $\partial\Omega_q$ where the metal ion flux \mathbf{J}_M or the hydrogen flux \mathbf{J}_H is known (Neumann-type boundary conditions), and $\partial\Omega_c$, where the metal ion concentration c_M or hydrogen concentration c_H is prescribed (Dirichlet-type boundary conditions). Note that we define $c_M = c'_M/c_{\text{solid}}$ as the normalised concentration, ranging from 0 to 1, with c'_M being the molar concentration of the metal ion and c_{solid} being the molar concentration of the metal ion in the solid. Besides, we adopt a penalty approach to enforce that the hydrogen concentration at the electrolyte-solid interface corresponds to that of the environment, $c_H = c_{\text{env}}$ (Martínez-Pañeda et al., 2020). This emulates how the newly created corrosion and crack surfaces are promptly exposed to the aqueous environment. The transport of species is driven by the chemical potential μ and, accordingly, we define a scalar field η to determine the kinematics of composition changes (Duda et al., 2018), such that

$$\dot{\eta} = \mu \quad \text{and} \quad \eta(\mathbf{x}, t) = \int_0^t \mu(\mathbf{x}, t) dt, \quad \text{for both } \mu_M \text{ and } \mu_H . \quad (3)$$

Finally, the morphology of the evolving electrolyte-metal interface is characterised by two phase field variables; a dissolution phase field ϕ_d that captures the short-range corrosion reactions (atoms detaching), and a fracture phase field ϕ_f , which captures the creation of new surfaces due to the breaking of atomic bonds. In both cases, see Fig. 1, we assume that $\phi_d = \phi_f = 1$ corresponds to the solid, undamaged material points, while $\phi_d = \phi_f = 0$ in the electrolyte. As described below, both formulations are non-local, involving their respective phase field gradients ($\nabla\phi_d, \nabla\phi_f$) and micro-stress quantities work conjugate to those gradients (ζ_d, ζ_f). The formulation allows for defining phase field micro-tractions, f_d and f_f , and also for the prescription of initial conditions and Dirichlet-type boundary conditions on the phase field variables. Thus, the interface morphology at time $t = 0$ can be set by defining a suitable geometry or by defining an initial condition on the phase field variables.

2.2. Principle of virtual work and force balances

Let us now derive the local force balances from the Principle of Virtual Work (PVW). In consistency with the kinematic fields described in Section 2.1, we define a set of virtual fields as $(\delta \mathbf{u}, \delta \phi_d, \delta \eta_M, \delta \phi_f, \delta \eta_H)$. For an arbitrary part Ω , considering the boundary definitions in Fig. 1, the internal virtual work $\delta \mathcal{W}^{\text{int}}$ and external virtual work $\delta \mathcal{W}^{\text{ext}}$ are given by

$$\begin{aligned} \delta \mathcal{W}^{\text{int}}(\Omega; \delta \mathbf{u}, \delta \phi_d, \delta \eta_M, \delta \phi_f, \delta \eta_H) = & \int_{\Omega} (\boldsymbol{\sigma} : \text{sym} \nabla \delta \mathbf{u} + \omega_d \delta \phi_d + \zeta_d \cdot \nabla \delta \phi_d \\ & - \mathbf{J}_M \cdot \nabla \delta \eta_M + \omega_f \delta \phi_f + \zeta_f \cdot \nabla \delta \phi_f - \mathbf{J}_H \cdot \nabla \delta \eta_H) dV \end{aligned} \quad (4)$$

and

$$\begin{aligned} \delta \mathcal{W}^{\text{ext}}(\Omega; \delta \mathbf{u}, \delta \phi_d, \delta \eta_M, \delta \phi_f, \delta \eta_H) = & \int_{\partial \Omega} (\mathbf{T} \cdot \delta \mathbf{u} + f_d \delta \phi_d + f_f \delta \phi_f + q_M \delta \eta_M \\ & + q_H \delta \eta_H) dS + \int_{\Omega} (\mathbf{b}^{\text{ext}} \cdot \delta \mathbf{u} + f_d^{\text{ext}} \delta \phi_d + f_f^{\text{ext}} \delta \phi_f + q_M^{\text{ext}} \delta \eta_M + q_H^{\text{ext}} \delta \eta_H) dV \end{aligned} \quad (5)$$

where $\boldsymbol{\sigma}$ is the Cauchy stress tensor, \mathbf{b} is the body force vector and ω_d and ω_f denote the microstress quantities work conjugate to ϕ_d and ϕ_f , respectively. Note that, following Duda et al. (2018), we decompose the external work quantities into the contact interactions on $\partial \Omega$ and the distant interactions, which account for the interactions with all bodies external to Ω . The superscript \square^{ext} denotes the variables in the latter group. The interactions at a distance can be further divided into a non-inertial part that accounts for interactions of bodies accessible to observation, and an inertial part account for interactions with the remaining bodies. Here, we assume that \mathbf{b}^{ext} , f_d^{ext} and f_f^{ext} are purely non-inertial but we decompose q_M and q_H as follows:

$$q_M^{\text{ext}} = q_M^{\text{ni}} - \dot{c}_M c_{\text{solid}}, \quad q_H^{\text{ext}} = q_H^{\text{ni}} - \dot{c}_H \quad (6)$$

where the superscript \square^{ni} is used to denote the non-inertial parts. The second term on the right hand sides of (6) are the inertial parts of q_M and q_H , and correspond to the solute number densities. By inserting (6) into (5), the external virtual work $\delta \mathcal{W}^{\text{ext}}$ is naturally decomposed into a non-inertial part $\delta \mathcal{W}^{\text{ni}}$ and an inertial part $\delta \mathcal{W}^{\text{in}}$, as follows

$$\delta \mathcal{W}^{\text{ext}} = \delta \mathcal{W}^{\text{ni}} + \delta \mathcal{W}^{\text{in}} \quad (7)$$

with

$$\begin{aligned} \delta \mathcal{W}^{\text{ni}}(\Omega; \delta \mathbf{u}, \delta \phi_d, \delta \eta_M, \delta \phi_f, \delta \eta_H) = & \int_{\partial \Omega} (\mathbf{T} \cdot \delta \mathbf{u} + f_d \delta \phi_d + f_f \delta \phi_f + q_M \delta \eta_M \\ & + q_H \delta \eta_H) dS + \int_{\Omega} (\mathbf{b}^{\text{ni}} \cdot \delta \mathbf{u} + f_d^{\text{ni}} \delta \phi_d + f_f^{\text{ni}} \delta \phi_f + q_M^{\text{ni}} \delta \eta_M + q_H^{\text{ni}} \delta \eta_H) dV \end{aligned} \quad (8)$$

and

$$\delta\mathcal{W}^{\text{in}}(\Omega; \delta\mathbf{u}, \delta\phi_d, \delta\eta_M, \delta\phi_f, \delta\eta_H) = - \int_{\Omega} (\dot{c}_M c_{\text{solid}} \delta\eta_M + \dot{c}_H \delta\eta_H) dV \quad (9)$$

We proceed to introduce the principle of virtual work, such that

$$\delta\mathcal{W}^{\text{int}}(\Omega; \delta\mathbf{u}, \delta\phi_d, \delta\eta_M, \delta\phi_f, \delta\eta_H) = \delta\mathcal{W}^{\text{ext}}(\Omega; \delta\mathbf{u}, \delta\phi_d, \delta\eta_M, \delta\phi_f, \delta\eta_H) \quad (10)$$

Now, let us neglect all non-inertial parts such that $\mathbf{b}^{\text{ni}} = \mathbf{0}$ and $f_d^{\text{ni}} = f_f^{\text{ni}} = q_M^{\text{ni}} = q_H^{\text{ni}} = 0$. Then, combining (4)-(10) and following Gauss' divergence theorem, the equilibrium equations on Ω are obtained as,

$$\begin{aligned} & \int_{\Omega} \left\{ (\nabla \cdot \boldsymbol{\sigma}) \cdot \delta\mathbf{u} + (\nabla \cdot \boldsymbol{\zeta}_d - \omega_d) \delta\phi_d - (\nabla \cdot \mathbf{J}_M + \dot{c}_M c_{\text{solid}}) \delta\eta_M \right. \\ & \quad \left. + (\nabla \cdot \boldsymbol{\zeta}_f - \omega_f) \delta\phi_f - (\nabla \cdot \mathbf{J}_H + \dot{c}_H) \delta\eta_H \right\} dV \\ &= \int_{\partial\Omega} \left\{ (\boldsymbol{\sigma} \cdot \mathbf{n} - \mathbf{T}) \cdot \delta\mathbf{u} + (\boldsymbol{\zeta}_d \cdot \mathbf{n} - f_d) \delta\phi_d + (\mathbf{J}_M \cdot \mathbf{n} + q_M) \delta\eta_M \right. \\ & \quad \left. + (\boldsymbol{\zeta}_f \cdot \mathbf{n} - f_f) \delta\phi_f + (\mathbf{J}_H \cdot \mathbf{n} + q_H) \delta\eta_H \right\} dS \end{aligned} \quad (11)$$

Since the left-hand side of (11) must vanish for arbitrary variations, the equilibrium equations in Ω are obtained as,

$$\begin{aligned} \nabla \cdot \boldsymbol{\sigma} &= \mathbf{0} \\ \nabla \cdot \boldsymbol{\zeta}_d - \omega_d &= 0 \\ \dot{c}_M c_{\text{solid}} + \nabla \cdot \mathbf{J}_M &= 0 \\ \nabla \cdot \boldsymbol{\zeta}_f - \omega_f &= 0 \\ \dot{c}_H + \nabla \cdot \mathbf{J}_H &= 0 \end{aligned} \quad (12)$$

and the right-hand side of (11) provides the corresponding set of boundary conditions on $\partial\Omega$,

$$\begin{aligned} \mathbf{T} &= \boldsymbol{\sigma} \cdot \mathbf{n} \\ f_d &= \boldsymbol{\zeta}_d \cdot \mathbf{n} \\ q_M &= -\mathbf{J}_M \cdot \mathbf{n} \\ f_f &= \boldsymbol{\zeta}_f \cdot \mathbf{n} \\ q_H &= -\mathbf{J}_H \cdot \mathbf{n} \end{aligned} \quad (13)$$

2.3. Energy imbalance

The first two laws of thermodynamics for a continuum body within a dynamical process of specific internal energy \mathcal{E} and specific entropy Λ read (Gurtin et al., 2010),

$$\begin{aligned} \frac{d}{dt} \int_{\Omega} \mathcal{E} dV &= \dot{\mathcal{W}}^{\text{ni}} - \int_{\partial\Omega} \mathbf{Q} \cdot \mathbf{n} dS + \int_{\Omega} Q dV \\ \frac{d}{dt} \int_{\Omega} \Lambda dV &\geq - \int_{\partial\Omega} \frac{\mathbf{Q}}{T} \cdot \mathbf{n} dS + \int_{\Omega} \frac{Q}{T} dV \end{aligned} \quad (14)$$

where $\dot{\mathcal{W}}^{\text{ni}}$ is the non-inertial part of external power, \mathbf{Q} is the heat flux and Q is the heat absorption. Here we limit our discussion within isothermal condition $T = T_0$ such that (14) can be re-written as:

$$\frac{d}{dt} \int_{\Omega} \psi dV \leq \dot{\mathcal{W}}^{\text{ni}} \quad (15)$$

where $\psi = \mathcal{E} - T\Lambda$ is the free energy density. Replacing the virtual fields $(\delta \mathbf{u}, \delta \phi_d, \delta \eta_M, \delta \phi_f, \delta \eta_H)$ by realisable velocity fields $(\dot{\mathbf{u}}, \dot{\phi}_d, \mu_M, \dot{\phi}_f, \mu_H)$ in (4) and (5), one can reach

$$\frac{d}{dt} \int_{\Omega} \psi dV \leq \int_{\partial\Omega} \left(\mathbf{T} \cdot \dot{\mathbf{u}} + f_d \dot{\phi}_d + f_f \dot{\phi}_f + q_M \mu_M + q_H \mu_H \right) dS \quad (16)$$

Employing the divergence theorem and recalling the local balance equations (12)-(13), we find the equivalent point-wise version of (16) as,

$$\begin{aligned} \dot{\psi} - \boldsymbol{\sigma} : \dot{\boldsymbol{\varepsilon}} - \left(\omega_d \dot{\phi}_d + \zeta_d \cdot \nabla \dot{\phi}_d \right) + \left(\mu_M \dot{c}_M c_{\text{solid}} - \mathbf{J}_M \cdot \nabla \mu_M \right) \\ - \left(\omega_f \dot{\phi}_f + \zeta_f \cdot \nabla \dot{\phi}_f \right) + \left(\mu_H \dot{c}_H - \mathbf{J}_H \cdot \nabla \mu_H \right) \leq 0 \end{aligned} \quad (17)$$

2.4. Free energy density

We proceed to define the functional form of free energy density ψ in (17). The free energy can be decomposed into the mechanical free energy density ψ^m , the chemical free energy density ψ^{ch} , the dissolution interface energy density ψ^i , the fracture interface energy density ψ^f , and the hydrogen-chemical energy density ψ^H , such that

$$\psi = \psi^m + \psi^{ch} + \psi^i + \psi^f + \psi^H \quad (18)$$

2.4.1. Mechanical free energy density

As shown in Fig. 1, in combining phase field corrosion and phase field fracture concepts, we choose to retain their original form and thus define different degradation functions for dissolution (h_d) and fracture (h_f), such that

$$h_d(\phi_d) = -2\phi_d^3 + 3\phi_d^2 \quad \text{and} \quad h_f(\phi_f) = \phi_f^2 \quad (19)$$

Subsequently, ψ^m is defined as:

$$\psi^m = h_d(\phi_d) h_f(\phi_f) \psi_0^m - K \bar{V}_H (c_H - c_{H0}) \text{tr } \boldsymbol{\epsilon} \quad (20)$$

where the first term on the right hand side is aimed at capturing the joint effect of dissolution and damage on the mechanical free energy density. Here, K is the bulk modulus, \bar{V}_H is the partial molar volume of hydrogen in solid solution, and c_{H0} is the reference hydrogen concentration. For an elastic-plastic solid, the mechanical free energy density ψ_0^m of the undamaged solid is given by:

$$\psi_0^m = \psi_0^e + \psi_0^p = \frac{1}{2} \boldsymbol{\epsilon}^e : \mathbf{C}^e : \boldsymbol{\epsilon}^e + \int_0^t \boldsymbol{\sigma}_0 : \dot{\boldsymbol{\epsilon}}^p dt \quad (21)$$

where ψ_0^e and ψ_0^p respectively denote the elastic and plastic parts of the (undamaged) mechanical free energy density, \mathbf{C}^e is the linear elastic stiffness matrix, and $\boldsymbol{\sigma}_0$ is the Cauchy stress tensor for the undamaged solid.

2.4.2. Electrochemical energy density

We follow the KKS model (Kim et al., 1999) to define the chemical free energy density ψ^{ch} , assuming that each material point is a mix of both solid and liquid phases with different concentrations but similar chemical potentials, such that

$$\psi^{ch} = h_d(\phi_d) \psi^{ch,S} + [1 - h_d(\phi_d)] \psi^{ch,L} + wg(\phi_d) \quad (22)$$

and

$$c_M = h_d(\phi_d) c_M^S + [1 - h_d(\phi_d)] c_M^L \quad (23)$$

$$\frac{\partial \psi^{ch,S}(c_M^S)}{\partial c_M^S} = \frac{\partial \psi^{ch,L}(c_M^L)}{\partial c_M^L} \quad (24)$$

where $\psi^{ch,S}$ and $\psi^{ch,L}$ denote the free energy density terms associated with the solid and liquid phases, c_M^S and c_M^L denote the normalized concentrations of the co-existing solid and liquid phases, and w is the height of the double well potential $g(\phi_d) = \phi_d^2(1 - \phi_d)^2$. $\psi^{ch,S}$ and $\psi^{ch,L}$ are defined as (Mai et al., 2016):

$$\psi^{ch,S} = A(c_M^S - c_{Se})^2 \quad \text{and} \quad \psi^{ch,L} = A(c_M^L - c_{Le})^2 \quad (25)$$

where A is the free energy density curvature, and $c_{Se} = c_{\text{solid}}/c_{\text{solid}} = 1$ and $c_{Le} = c_{\text{sat}}/c_{\text{solid}}$ respectively denote the normalised equilibrium concentrations for the solid and liquid phases.

Combining (22)-(25) renders,

$$\psi^{ch} = A [c_M - h_d (\phi_d) (c_{Se} - c_{Le}) - c_{Le}]^2 + w \phi_d^2 (1 - \phi_d)^2. \quad (26)$$

2.4.3. Dissolution interface energy density

The dissolution interface energy density ψ^i is defined as a function of the gradient of the corrosion phase field order parameter ϕ_d as:

$$\psi^i = \frac{\alpha}{2} |\nabla \phi_d|^2 \quad (27)$$

where α is the gradient energy coefficient. The parameters α and w in the electrochemical system (26)-(27) are related to the interface energy γ and its thickness ℓ_d , rendering

$$\gamma = \sqrt{\frac{\alpha w}{18}} \quad \text{and} \quad \ell_d = a^* \sqrt{\frac{2\alpha}{w}} \quad (28)$$

where $a^* = 2.94$ is a constant parameter corresponding to the definition of the interface region $0.05 < \phi < 0.95$ (Abubakar et al., 2015).

2.4.4. Fracture interface energy density

The phase field description of the fracture problem is aimed at regularising Griffith's energy balance and determine the evolution of ϕ_f based on the thermodynamics of fracture (Bourdin et al., 2008). Accordingly, for a material toughness G_c , the fracture interface energy density ψ^f is given by,

$$\psi^f = G_c (c_H) \left[\frac{\ell_f}{2} |\nabla \phi_f|^2 + \frac{1}{2\ell_f} (1 - \phi_f)^2 \right] \quad (29)$$

where ℓ_f is the length scale parameter, governing the size of the regularised region. As shown in (29), the role of hydrogen in degrading the fracture resistance of the solid is introduced by making the critical energy release rate sensitive to the hydrogen content. The formulation is general, in that it can incorporate any definition of the toughness degradation to accommodate any mechanistic interpretation. One possibility, as presented by Martínez-Pañeda et al. (2018), is to adopt an atomistically-informed approach, by which the fracture energy degradation is related to atomistic computations of surface energy sensitivity to hydrogen coverage, θ . The hydrogen coverage at an interface can be estimated by means of the Langmuir–McLean isotherm (Serebrinsky et al., 2004):

$$\theta = \frac{c_H}{c_H + \exp\left(\frac{-\Delta g_b^0}{RT}\right)} \quad (30)$$

where R is the universal gas constant and Δg_b^0 is the interface binding energy. For example, for hydrogen assisted failures driven by grain boundary decohesion (Harris et al., 2018), Δg_b^0 corresponds to the binding energy of grain boundaries, which is on the order of 30 kJ/mol. As noted by Martínez-Pañeda et al. (2018), atomistic calculations of surface energy degradation with increasing hydrogen coverage can be approximated with a linear trend, such that:

$$G_c(c_H) = G_c(\theta) = (1 - \chi\theta) G_c(0) \quad (31)$$

where χ is the so-called hydrogen damage coefficient. For Fe-based materials, $\chi = 0.89$ provides the best fit to the data by Jiang and Carter (2004), while $\chi = 0.41$ provides the best fit to the DFT simulations on Ni by Alvaro et al. (2015). In this work, we will make use of this atomistically-informed approach to provide fully predictive estimates (i.e., without the need for experimental calibration) but we will also consider phenomenological approaches and discuss their differences.

2.4.5. Hydrogen-chemical energy density

Hydrogen transport is driven by chemical potential gradients. For a given number of hydrogen sites N_H with occupancy $\theta_H = c_H/N_H$, the hydrogen-chemical energy density is given by (Kristensen et al., 2020a):

$$\psi^H = \mu_0 c_H + RT N_H [\theta_H \ln \theta_H + (1 - \theta_H) \ln (1 - \theta_H)] \quad (32)$$

where μ_0 is the reference chemical potential. The formulation is general in that it can refer to the transport of lattice hydrogen or to the transport of diffusible hydrogen, upon appropriate choices of the hydrogen diffusion coefficient D_H . Thus, the role of microstructural trapping sites can be accounted for in the present formulation, both in terms of their involvement in the fracture process (see Section 2.4.4) and in their role in reducing diffusion rates, through a suitable choice of D_H . For simplicity, we do not capture the effect of an evolving trap density, as it is the case of dislocation trap sites, but such extension is straightforward (see Isfandbod and Martínez-Pañeda, 2021).

2.5. Constitutive theory

Let us now outline our constitutive choices, consistent with the free energy imbalance (Section 2.3) and the free energy definition (Section 2.4). First, following Anand and co-workers (see,

e.g. Narayan and Anand, 2019; Anand et al., 2019), the dissipative nature of the corrosion and fracture processes is emphasised by decomposing the dissolution and fracture micro-stresses into energetic and dissipative parts:

$$\omega_d = \omega_d^{\text{en}} + \omega_d^{\text{dis}} \quad \text{and} \quad \omega_f = \omega_f^{\text{en}} + \omega_f^{\text{dis}}. \quad (33)$$

Accordingly, the constitutive relations can be derived by fulfilling the free energy imbalance:

$$\begin{aligned} & \left(\frac{\partial \psi}{\partial \boldsymbol{\varepsilon}} - \boldsymbol{\sigma} \right) : \dot{\boldsymbol{\varepsilon}} + \left(\frac{\partial \psi}{\partial \phi_d} - \omega_d^{\text{en}} \right) \dot{\phi}_d + \left(\frac{\partial \psi}{\partial \nabla \phi_d} - \zeta_d \right) \nabla \dot{\phi}_d \\ & + \left[\left(\frac{\partial \psi}{\partial c_M} + \mu_M c_{\text{solid}} \right) \dot{c}_M - \mathbf{J}_M \cdot \nabla \mu_M \right] + \left(\frac{\partial \psi}{\partial \phi_f} - \omega_f^{\text{en}} \right) \dot{\phi}_f \\ & + \left(\frac{\partial \psi}{\partial \nabla \phi_f} - \zeta_f \right) \nabla \dot{\phi}_f + \left[\left(\frac{\partial \psi}{\partial c_H} + \mu_H \right) \dot{c}_H - \mathbf{J}_H \cdot \nabla \mu_H \right] \leq 0 \end{aligned} \quad (34)$$

with free energy ψ being defined, in agreement with Section 2.4, as follows:

$$\begin{aligned} \psi = \psi(\boldsymbol{\varepsilon}, \phi_d, c_M, \phi_f, c_H) = & \underbrace{[h_d(\phi_d) h_f(\phi_f) \psi_0^m - K \bar{V}_H (c_H - c_{H0}) \text{tr} \boldsymbol{\varepsilon}]}_{\psi^m} \\ & + \underbrace{A [c_M - h_d(\phi_d) (c_{\text{Se}} - c_{\text{Le}}) - c_{\text{Le}}]^2 + w \phi_d^2 (1 - \phi_d)^2}_{\psi^{ch}} \\ & + \underbrace{\frac{\alpha}{2} |\nabla \phi_d|^2}_{\psi^i} + \underbrace{G_c(c_H) \left[\frac{\ell_f}{2} |\nabla \phi_f|^2 + \frac{1}{2 \ell_f} (1 - \phi_f)^2 \right]}_{\psi^f} \\ & + \underbrace{\mu_0 c_H + RT N_H [\theta_H \ln \theta_H + (1 - \theta_H) \ln (1 - \theta_H)]}_{\psi^H} \end{aligned} \quad (35)$$

Here, one should note that ω_d^{dis} and ω_f^{dis} must obey the following residual dissipation inequality,

$$\omega_d^{\text{dis}} \geq 0 \quad \text{and} \quad \omega_f^{\text{dis}} \geq 0 \quad (36)$$

The general formulations of the dissipative microstress quantities are given by:

$$\omega_d^{\text{dis}} = \hat{a}(\boldsymbol{\varepsilon}, \phi_d, \nabla \phi_d, \eta_M, \phi_f, \nabla \phi_f, \eta_H) + \hat{b}(\boldsymbol{\varepsilon}, \phi_d, \nabla \phi_d, \eta_M, \phi_f, \nabla \phi_f, \eta_H) \dot{\phi}_d. \quad (37)$$

$$\omega_f^{\text{dis}} = \hat{\alpha}(\boldsymbol{\varepsilon}, \phi_d, \nabla \phi_d, \eta_M, \phi_f, \nabla \phi_f, \eta_H) + \hat{\beta}(\boldsymbol{\varepsilon}, \phi_d, \nabla \phi_d, \eta_M, \phi_f, \nabla \phi_f, \eta_H) \dot{\phi}_f. \quad (38)$$

where \hat{a} , \hat{b} , $\hat{\alpha}$, and $\hat{\beta}$ are non-negative response functions to ensure satisfying of (36). Particularly, the conditions $\hat{b} = 0$ and $\hat{\beta} = 0$ correspond to rate-independent processes. For simplicity, we follow Duda et al. (2015) and assume $\hat{a} = \hat{\alpha} = 0$.

2.5.1. Chemo-elastoplasticity

The constitutive prescriptions for the mechanical behaviour of the solid are derived as follows. According to (34) and (35), the Cauchy stress tensor can be derived as:

$$\boldsymbol{\sigma} = \frac{\partial \psi}{\partial \boldsymbol{\varepsilon}} = h_d(\phi_d) h_f(\phi_f) \mathbf{C}^{\text{ep}} : \boldsymbol{\varepsilon} - K \bar{V}_H (c_H - c_{H0}) \text{tr} \mathbf{I} \quad (39)$$

where $\mathbf{C}^{\text{ep}} = \partial \boldsymbol{\sigma} / \partial \boldsymbol{\varepsilon}$ is the consistent material Jacobian. The second term, corresponding to lattice dilation, is considered to have a negligible effect in hydrogen embrittlement phenomena (Hirth, 1980) and is subsequently omitted.

The work hardening behaviour of the solid is assumed to be characterised by an isotropic power law, such that the relation between the flow stress σ and the equivalent plastic strain ε^p is given by,

$$\sigma = \sigma_y \left(1 + \frac{E \varepsilon^p}{\sigma_y} \right)^N \quad (40)$$

where E is Young's modulus, σ_y is the initial yield stress and N is the strain hardening exponent ($0 \leq N \leq 1$).

For simplicity, we have chosen to describe the constitutive behaviour of the solid using J_2 plasticity theory. The framework can readily be incorporated to capture the role of crystal anisotropy (Castelluccio et al., 2018; Kumar and Mahajan, 2020; Tondro and Abdolvand, 2021) and dislocation hardening due to plastic strain gradients (Komaragiri et al., 2008; Martínez-Pañeda and Fleck, 2019; Martínez-Pañeda et al., 2019). The former is mostly relevant for predicting pit nucleation and the growth of very small cracks (smaller than a characteristic microstructural length). While strain gradient effects become most important in pre-cracked samples exposed to anodic environments, as strain gradient hardening will lead to higher hydrogen contents.

2.5.2. A phase field description of metallic corrosion

The evolution of the corrosion front is characterised by the dissolution phase field microstress vector ζ_d , work conjugate to the phase field gradient,

$$\zeta_d = \frac{\partial \psi}{\partial \nabla \phi_d} = \alpha \nabla^2 \phi_d, \quad (41)$$

and the scalar micro-stress ω_d , work conjugate to the dissolution phase field ϕ_d . In agreement with (35), the energetic part of ω_d is defined as follows:

$$\begin{aligned} \omega_d^{\text{en}} = \frac{\partial \psi}{\partial \phi_d} = & -2A [c_M - h_d(\phi_d) (c_{\text{Se}} - c_{\text{Le}}) - c_{\text{Le}}] (c_{\text{Se}} - c_{\text{Le}}) h'_d(\phi_d) \\ & + w (4\phi_d^3 + 2\phi_d - 6\phi_d^2) + h'_d(\phi_d) h_f(\phi_f) \psi_0^m \end{aligned} \quad (42)$$

The last term in (42) makes corrosion kinetics sensitive to the mechanical fields, as shown by Nguyen et al. (2017, 2018). This term requires careful consideration. Corrosion is a rate-dependent process which can be either activation-controlled or diffusion-controlled, with the role of mechanical fields in enhancing the local current density being only relevant under activation-controlled corrosion (Gutman, 1998). However, the last term in (42) leads to an influence of mechanical fields in corrosion kinetics even under diffusion-controlled conditions, where corrosion is only governed by ionic transport. Hence, we drop this term and, instead, account for the interplay between metal dissolution and mechanics *via* the dissipative microstress ω_d^{dis} . In the application of the phase field paradigm to metallic corrosion, dissipation is governed by the interface kinetics coefficient L , also referred to as the mobility parameter. Accordingly, the dissipative part of the corrosion micro-stress is given by

$$\omega_d^{\text{dis}} = \hat{b} \dot{\phi}_d = \frac{1}{L} \dot{\phi}_d. \quad (43)$$

Following the work by Cui et al. (2021), the mobility parameter is made dependent of the mechanical fields to incorporate two important effects: (i) the role of mechanical straining in rupturing the protective passive film, and (ii) the role of mechanical fields in enhancing corrosion kinetics. The former is accounted for in agreement with the film-rupture-dissolution-repassivation (FRDR) mechanism (Parkins, 1987), while the latter is introduced following Gutman (1998) mechanochemical theory. Accordingly, the mechanics-enhanced mobility coefficient is defined as,

$$L(\varepsilon^p, \sigma_h) = \begin{cases} k_m(\varepsilon^p, \sigma_h) L_0, & \text{if } 0 < t_i \leq t_0 \\ k_m(\varepsilon^p, \sigma_h) L_0 \exp(-k(t_i - t_0)), & \text{if } t_0 < t_i \leq t_0 + t_f \end{cases} \quad (44)$$

where σ_h is the hydrostatic stress, L_0 is the reference mobility coefficient (in the absence of mechanical straining) and k_m denotes the mechanochemical term. Following Gutman (1998), the mechanochemical term is defined as follows to capture the impact of mechanical fields on corrosion kinetics,

$$k_m(\varepsilon^p, \sigma_h) = \left(\frac{\varepsilon^p}{\varepsilon_y} + 1 \right) \exp\left(\frac{\sigma_h V_m}{RT} \right), \quad (45)$$

where $\varepsilon_y = \sigma_y/E$ is the yield strain and V_m is the molar volume. In regard to the cyclic film-rupture process, as elaborated in Cui et al. (2021), the upper part of (44) corresponds to the behaviour when the passive film has been ruptured and thus the corrosion current density and L take their highest values (bare metal corrosion). After a time t_0 , repassivation starts to play a

role and reduces the current density (and L). The rate of decay depends on the stability of the passive film, the material and the environment, and is characterised through the parameter k . The exponential shape of (44)b reflects the increase in film stability with time that is observed as more oxides are deposited. After a time t_f since the decay process started, a rupture event occurs and again $L = k_m L_0$. Film rupture is governed by a competition between repassivation kinetics, how long it takes for a film to stabilise, and crack tip straining, how fast the new film will accumulate strains until reaching a critical value. Accordingly, film rupture will occur when the accumulated equivalent plastic strain over a FRDR cycle ε_i^p reaches a critical failure strain ε_f ,

$$\varepsilon_i^p = \varepsilon_f \quad \text{with} \quad \varepsilon_i^p = \int_0^{t_i} \varepsilon^p dt \quad (46)$$

where the total time for each FRDR cycle equals $t_i = t_0 + t_f$ and ε_f is assumed to be on the order of 0.1% (Gutman, 2007).

Finally, insert these constitutive relations (33), (41)-(43), into the phase field balance equation (12b), to re-formulate the strong form as:

$$\frac{1}{L(\varepsilon^p, \sigma_h)} \frac{d\phi_d}{dt} + \left(\frac{\partial \psi^{ch}}{\partial \phi_d} - \alpha \nabla^2 \phi_d \right) = 0, \quad (47)$$

with

$$\frac{\partial \psi^{ch}}{\partial \phi_d} = -2A [c_M - h_d(\phi_d)(c_{Se} - c_{Le}) - c_{Le}] (c_{Se} - c_{Le}) h'_d(\phi_d) + w g'(\phi_d) \quad (48)$$

2.5.3. Transport of ionic species

Let us now derive the constitutive prescriptions for the transport of metallic ions, which governs corrosion under diffusion-controlled conditions. Following (34)-(35), the chemical potential μ_M is given by,

$$\mu_M = \frac{1}{c_{solid}} \frac{\partial \psi}{\partial c_M} = \frac{2A}{c_{solid}} [(c_M - h_d(\phi_d)(c_{Se} - c_{Le}) - c_{Le})] \quad (49)$$

While the flux \mathbf{J}_M can be determined following a Fick law-type relation as,

$$\mathbf{J}_M = -\frac{D_M}{2A} \cdot c_{solid} \cdot c_{solid} \cdot \nabla \mu_M = c_{solid} \cdot D_M \nabla [(c_M - h_d(\phi_d)(c_{Se} - c_{Le}) - c_{Le})] \quad (50)$$

where D_M is the diffusion coefficient of metal ion. Finally, inserting (49) and (50) into the mass transport balance (12c), one can subsequently obtain the following governing equation for metal ion diffusion:

$$\frac{dc_M}{dt} - \nabla \cdot D_M \nabla [(c_M - h_d(\phi_d)(c_{Se} - c_{Le}) - c_{Le})] = 0 \quad (51)$$

2.5.4. A phase field description of fracture

We now turn our attention to the constitutive relations for phase field fracture. The energetic microstress ω_f^{en} in (34) is given by:

$$\omega_f^{\text{en}} = \frac{\partial \psi}{\partial \phi_f} = h'_f(\phi_f) h_d(\phi_d) \psi_0^m - G_c(c_H) \frac{1 - \phi_f}{\ell_f} \quad (52)$$

Here, fracture is assumed to be a rate-independent process such that $\hat{\beta} = 0$ in (38). In addition, the phase field microstress vector ζ_f reads:

$$\zeta_f = \frac{\partial \psi}{\partial \nabla \phi_f} = G_c(c_H) \ell_f \nabla \phi_f \quad (53)$$

Inserting (52)-(53) into the phase field local balance (12d), the phase field fracture balance equation can be formulated as:

$$h'_f(\phi_f) h_d(\phi_d) \psi_0^m + G_c(c_H) \left(-\frac{1 - \phi_f}{\ell_f} - \ell_f \nabla^2 \phi_f \right) = 0, \quad (54)$$

where, as in Martínez-Pañeda et al. (2018), we have assumed that the concentration gradient is small at the interface.

2.5.5. Diffusion of atomic hydrogen

We conclude the description of our constitutive theory by deriving the appropriate relations for hydrogen transport. In agreement with (34)-(35), the chemical potential is given by,

$$\mu_H = \frac{\partial \psi}{\partial c_H} = \mu_0 + RT \ln \frac{\theta_H}{1 - \theta_H} - \bar{V}_H \sigma_h + \frac{dG_c(c_H)}{dc_H} \frac{d\theta}{d\theta} \left[\frac{\ell_f}{2} |\nabla \phi_f|^2 + \frac{1}{2\ell_f} (1 - \phi_f)^2 \right] \quad (55)$$

The last term in (55), which enhances hydrogen transport from damaged regions to pristine regions, is neglected as a penalty-based *moving* chemical boundary condition is implemented to capture how the aqueous solution immediately occupies the space created by crack advance (Martínez-Pañeda et al., 2020). Accordingly, the hydrogen flux \mathbf{J}_H is determined through a linear Onsager relationship,

$$\mathbf{J}_H = -\frac{D_H c_H}{RT} \nabla \mu_H = -\frac{D_H c_H}{\theta_H (1 - \theta_H)} \nabla \theta_H + \frac{D_H c_H}{RT} \bar{V}_H \nabla \sigma_h \quad (56)$$

which, under the common assumption of low occupancy ($\theta_H \ll 1$), reads

$$\mathbf{J}_H = -D_H \nabla c_H + \frac{D_H c_H}{RT} \bar{V}_H \nabla \sigma_h \quad (57)$$

Inserting (55) and (57) into the hydrogen transport balance (12e), the strong form of the atomic hydrogen diffusion problem becomes:

$$\frac{dc_H}{dt} - D_H \nabla c_H + \frac{D_H c_H}{RT} \bar{V}_H \nabla \sigma_h = 0 \quad (58)$$

2.6. Summary of the governing equations

2.6.1. Strong form and multi-physics interactions

Our formulation resolves five key physical processes, namely mechanical deformation, metal dissolution, ionic transport, fracture, and hydrogen diffusion. We shall now summarise the governing equations obtained for the associated primal field quantities (\mathbf{u} , ϕ_d , c_M , ϕ_f , c_H), see Table 1, and discuss their interactions.

Table 1: Summary of the strong form of the governing equations of the model.

Governing equations:

$$\nabla \cdot \boldsymbol{\sigma} = \mathbf{0} \quad (\text{T.1})$$

$$\frac{1}{L(\varepsilon^p, \sigma_h)} \frac{d\phi_d}{dt} + \left(\frac{\partial \psi^{ch}}{\partial \phi_d} - \alpha \nabla^2 \phi_d \right) = 0 \quad (\text{T.2})$$

$$\frac{dc_M}{dt} - \nabla \cdot D_M \nabla [(c_M - h_d(\phi_d)(c_{Se} - c_{Le}) - c_{Le})] = 0 \quad (\text{T.3})$$

$$h'_f(\phi_f) h_d(\phi_d) \psi_0^m + G_c(c_H) \left(-\frac{1-\phi_f}{\ell_f} - \ell_f \nabla^2 \phi_f \right) = 0 \quad (\text{T.4})$$

$$\frac{dc_H}{dt} - D_H \nabla c_H + \frac{D_H c_H}{RT} \bar{V}_H \nabla \sigma_h = 0 \quad (\text{T.5})$$

with:

$$\boldsymbol{\sigma} = \frac{\partial \psi}{\partial \boldsymbol{\varepsilon}} = h_d(\phi_d) h_f(\phi_f) \mathbf{C}^{ep} : \text{sym} \nabla \mathbf{u} \quad (\text{T.6})$$

$$\frac{\partial \psi^{ch}}{\partial \phi_d} = -2A [c_M - h_d(\phi_d)(c_{Se} - c_{Le}) - c_{Le}] (c_{Se} - c_{Le}) h'_d(\phi_d) + w g'(\phi_d) \quad (\text{T.7})$$

$$\psi_0^m = \frac{1}{2} \boldsymbol{\varepsilon}^e : \mathbf{C}^e : \boldsymbol{\varepsilon}^e + \int_0^t \boldsymbol{\sigma}_0 : \dot{\boldsymbol{\varepsilon}}^p dt \quad (\text{T.8})$$

These governing equations account for multiple coupling phenomena, as described below.

- Metal dissolution and ionic transport

When diffusion-controlled corrosion conditions are relevant (i.e., a sufficiently large L), the evolution of ϕ_d is driven by the concentration of metal ions - see the first term on the right hand side of (T.7). Also, as shown in (T.3), the dissolution phase field interacts with the ionic transport equation; the diffusion of metal ions is restricted by ϕ_d such that it only takes place along the corrosion interface and in the electrolyte.

- Metal dissolution and mechanical fields

The dissolution process redistributes mechanical fields by reducing the stiffness of the solid through a degradation function $h_d(\phi_d)$, see (T.6). Additionally, the mechanical fields impact the corrosion behaviour in two ways: (i) by enhancing corrosion kinetics, and (ii) by breaking the protective passive film. Both effects are incorporated by defining the mobility coefficient dependent on the relevant mechanical quantities, $L = L(\varepsilon^p, \sigma_h)$ - see (T.2) and (44).

- Metal dissolution and fracture

The interaction of metal dissolution and physical fracture is implemented by defining a joint degradation term $h_d(\phi_d) \cdot h_f(\phi_f)$, see (T.6). As a result, metal dissolution provides an additional term to the conventional phase field fracture balance equation, preventing cracks from nucleating in the electrolyte, see (T.4). On the other hand, no action is taken to prevent corrosion from happening in cracked regions due to the very different time scales involved and the fact that corrosion typically precedes structural failure. For visualisation purposes, an equivalent damage variable ϕ_e is defined to describe the joint effect of dissolution and fracture damage: $\phi_e = \phi_d \cdot \phi_f$.

- Mechanical fields and hydrogen diffusion

Mechanical fields and hydrogen transport are coupled in one direction as higher hydrostatic stresses (volumetric strains) drive hydrogen transport due to lattice dilation; this is accounted for by the last term in (T.5). Thus, hydrogen accumulates ahead of pits, cracks and other defects.

- Fracture and hydrogen diffusion

There is a two-way interaction between hydrogen diffusion and fracture. First, the material toughness is defined to be a function of the hydrogen content $G_c(c_H)$, see (T.4). This captures the embrittlement effect of hydrogen. Second, as detailed below, a penalty approach is used to enforce $c_H = c_{\text{env}}$ in cracked regions, where c_{env} is the hydrogen content associated with the environment.

2.6.2. A brief discussion on ℓ_d and ℓ_f

The proposed multi-phase-field formulation incorporates two length scale parameters, ℓ_d for the dissolution process and ℓ_f for the fracture process. Both provide a measure of the interface

thickness. In the case of phase field corrosion, ℓ_d is not an explicit parameter but a byproduct of the height of the double well potential w and the gradient energy coefficient α - see (28). The interface energy γ and the thickness of the reaction interface ℓ_d can, in principle, be estimated from experiments (Abubakar et al., 2015) and, consequently, w and α can be determined as follows:

$$w = \frac{6\gamma a^*}{\ell_d} \quad \text{and} \quad \alpha = \frac{3\gamma\ell_d}{a^*}. \quad (59)$$

Regarding the phase field fracture length scale, ℓ_f ; it can be seen as a regularising parameter in the limit $\ell_f \rightarrow 0^+$ but it is generally considered to be a material parameter that defines the material strength σ_c (Tanné et al., 2018; Kristensen et al., 2021). This can be readily observed by considering the homogeneous solution to (54), giving a maximum stress of:

$$\sigma_c = \frac{3}{16} \sqrt{\frac{3EG_c}{\ell_f}}. \quad (60)$$

3. Numerical implementation

We proceed to briefly describe the details of the numerical implementation, including the formulation of the weak form (Section 3.1), the finite element discretisation (Section 3.2) and the derivation of the residuals and stiffness matrices (Section 3.3).

3.1. Weak form

The weak form of the balance equations in Table 1 can be readily derived as:

$$\int_{\Omega} [h_d(\phi_d) h_f(\phi_f) + \kappa] \boldsymbol{\sigma}_0 \delta \boldsymbol{\varepsilon} \, dV - \int_{\partial\Omega} \mathbf{T} \cdot \delta \mathbf{u} \, dS = 0 \quad (61)$$

$$\int_{\Omega} \frac{1}{L(\varepsilon^p, \sigma_h)} \frac{d\phi_d}{dt} \delta \phi_d \, dV + \int_{\Omega} \frac{\partial \psi^{ch}}{\partial \phi_d} \delta \phi_d \, dV + \int_{\Omega} \alpha \nabla \phi_d \cdot \nabla \delta \phi_d \, dV = 0 \quad (62)$$

$$\int_{\Omega} \frac{1}{D_M} \frac{dc_M}{dt} \delta c_M \, dV + \int_{\Omega} \nabla [c_M - h_d(\phi_d) (c_{Se} - c_{Le}) - c_{Le}] \cdot \nabla \delta c_M \, dV = 0 \quad (63)$$

$$\int_{\Omega} h'_f(\phi_f) h_d(\phi_d) \mathcal{H} \, dV + \int_{\Omega} G_c(c_H) \left(-\frac{1-\phi_f}{\ell_f} \delta \phi_f + \ell_f \nabla \phi_f \cdot \nabla \delta \phi_f \right) \, dV = 0 \quad (64)$$

$$\int_{\Omega} \frac{1}{D_H} \frac{dc_H}{dt} \delta c_H \, dV + \int_{\Omega} \nabla c_H \cdot \nabla \delta c_H \, dV - \int_{\Omega} \frac{\bar{V}_{HCH}}{RT} \nabla \sigma_h \cdot \nabla \delta c_H \, dV = 0 \quad (65)$$

where $\kappa = 1 \times 10^{-5}$ is a parameter chosen to keep the system of equations well-conditioned and \mathcal{H} is the driving force for fracture, which incorporates a history variable field to ensure damage irreversibility (Miehe et al., 2010). Since the effective plastic work increases monotonically, the irreversibility condition is only applied to the elastic part. Thus, in its most general form, the driving force for fracture is given by,

$$\mathcal{H} = \beta_e \mathcal{H}^e + \beta_p \psi_0^p = \beta_e \max_{\tau \in [0, t]} \psi_0^{e+}(\tau) + \beta_p \psi_0^p. \quad (66)$$

where β_e and β_p are weighting factors (Borden et al., 2016), which are taken to be equal to 1, unless otherwise stated. Also, ψ_0^{e+} refers to the tensile part of the elastic free energy density; $\psi_0^e = \psi_0^{e+} + \psi_0^{e-}$. This decomposition is applied to prevent damage under compression, and we choose to adopt the so-called spherical/deviatoric split (Amor et al., 2009),

$$\psi_0^{e+} = \frac{1}{2} K \langle \text{tr}(\boldsymbol{\varepsilon}^e) \rangle_+^2 + \mu (\boldsymbol{\varepsilon}^{e'} : \boldsymbol{\varepsilon}^{e'}) \quad \text{and} \quad \psi_0^{e-} = \frac{1}{2} K \langle \text{tr}(\boldsymbol{\varepsilon}^e) \rangle_-^2 \quad (67)$$

where $\langle \square \rangle$ denote Macaulay brackets and μ is the shear modulus.

3.2. Finite element discretisation

The finite element method is used to discretise and solve the coupled equations (61)-(65). Using Voigt's notation, the nodal variables for the displacement field $\hat{\mathbf{u}}$, the phase field corrosion order parameter $\hat{\phi}_d$, the normalised metal ion concentration \hat{c}_M , the phase field fracture order parameter $\hat{\phi}_f$, and the hydrogen concentration \hat{c}_H are interpolated as:

$$\mathbf{u} = \sum_{i=1}^m \mathbf{N}_i^{\mathbf{u}} \hat{\mathbf{u}}_i, \quad \phi_d = \sum_{i=1}^m N_i \hat{\phi}_{d_i}, \quad c_M = \sum_{i=1}^m N_i \hat{c}_{M_i}, \quad \phi_f = \sum_{i=1}^m N_i \hat{\phi}_{f_i}, \quad c_H = \sum_{i=1}^m N_i \hat{c}_{H_i} \quad (68)$$

where N_i denotes the shape function associated with node i , for a total number of nodes m , and $\mathbf{N}_i^{\mathbf{u}}$ is a diagonal interpolation matrix with the nodal shape functions N_i as components. Similarly, using the standard strain-displacement \mathbf{B} matrices, the associated gradient quantities are discretised as:

$$\boldsymbol{\varepsilon} = \sum_{i=1}^m \mathbf{B}_i^{\mathbf{u}} \hat{\mathbf{u}}_i, \quad \nabla \phi_d = \sum_{i=1}^m \mathbf{B}_i \hat{\phi}_{d_i}, \quad \nabla c_M = \sum_{i=1}^m \mathbf{B}_i \hat{c}_{M_i}, \quad \nabla \phi_f = \sum_{i=1}^m \mathbf{B}_i \hat{\phi}_{f_i}, \quad \nabla c_H = \sum_{i=1}^m \mathbf{B}_i \hat{c}_{H_i} \quad (69)$$

3.3. Residuals and stiffness matrices

Considering the finite element discretisation (68)-(69), the weak form equations (61)-(65) can be discretised to derive the following residuals,

$$\mathbf{r}_i^{\mathbf{u}} = \int_{\Omega} [h_d(\phi_d) h_f(\phi_f) + \kappa] (\mathbf{B}_i^{\mathbf{u}})^T \boldsymbol{\sigma}_0 dV - \int_{\partial\Omega} (\mathbf{N}_i^{\mathbf{u}})^T \mathbf{T} dS \quad (70)$$

$$r_i^{\phi_d} = \int_{\Omega} \frac{1}{L(\varepsilon^p, \sigma_h)} \frac{d\phi_d}{dt} N_i dV + \int_{\Omega} \frac{\partial \psi^{ch}}{\partial \phi_d} N_i dV + \int_{\Omega} \alpha \mathbf{B}_i^T \nabla \phi_d dV \quad (71)$$

$$r_i^{\text{cM}} = \int_{\Omega} \frac{1}{D_M} \frac{dc_M}{dt} N_i dV + \int_{\Omega} \mathbf{B}_i^T [\nabla c_M - h'_d(\phi_d)(c_{\text{Se}} - c_{\text{Le}}) \nabla \phi_d] dV \quad (72)$$

$$r_i^{\phi_f} = \int_{\Omega} h'_f(\phi_f) h_d(\phi_d) N_i \mathcal{H} dV + G_c(c_H) \int_{\Omega} \left(-\frac{1 - \phi_f}{\ell_f} N_i + \ell_f \mathbf{B}_i^T \nabla \phi_f \right) dV \quad (73)$$

$$r_i^{\text{cH}} = \int_{\Omega} \left[\frac{1}{D_H} \frac{dc_H}{dt} + (c_H - c_{\text{env}}) \langle 1 - 2\phi_d \phi_f \rangle k_p \right] N_i dV + \int_{\Omega} \mathbf{B}_i^T \nabla c_H dV - \int_{\Omega} \mathbf{B}_i^T \left(\frac{\bar{V}_H c_H}{RT} \right) \nabla \sigma_h dV \quad (74)$$

where k_p is a penalty factor to enforce $c_H = c_{\text{env}}$ when $\phi_d \phi_f$ approaches zero, the moving chemical boundary conditions that mimic the prompt exposure of newly created defect surfaces to the environment (Martínez-Pañeda et al., 2020). Specifically, we find that a linear transition from $\phi_d \phi_f = 0.5$ and a k_p value of 10^5 adequately enforce $c_H = c_{\text{env}}$ while providing good numerical stability. Accordingly, the tangent stiffness matrices are then calculated as:

$$\mathbf{K}_{ij}^{\mathbf{u}} = \int_{\Omega} [h_d(\phi_d) h_f(\phi_f) + \kappa] (\mathbf{B}_i^{\mathbf{u}})^T \mathbf{C}_{\text{ep}} \mathbf{B}_j^{\mathbf{u}} dV \quad (75)$$

$$\mathbf{K}_{ij}^{\phi_d} = \int_{\Omega} \frac{1}{L(\varepsilon^p, \sigma_h)} \frac{N_i^T N_j}{dt} dV + \int_{\Omega} \frac{\partial^2 \psi^{ch}}{\partial \phi_d^2} N_i^T N_j dV + \int_{\Omega} \alpha \mathbf{B}_i^T \mathbf{B}_j dV \quad (76)$$

$$\mathbf{K}_{ij}^{\text{cM}} = \int_{\Omega} \frac{1}{D_M} \frac{N_i^T N_j}{dt} dV + D_M \int_{\Omega} \mathbf{B}_i^T \mathbf{B}_j dV \quad (77)$$

$$\mathbf{K}_{ij}^{\phi_f} = \int_{\Omega} \left\{ \left[h''_f(\phi_f) h_d(\phi_d) \mathcal{H} + \frac{G_c(c_H)}{\ell_f} \right] N_i^T N_j + G_c(c_H) \ell_f \mathbf{B}_i^T \mathbf{B}_j \right\} dV \quad (78)$$

$$\mathbf{K}_{ij}^{\text{cH}} = \int_{\Omega} \frac{1}{D_H} \frac{N_i^T N_j}{dt} dV + \int_{\Omega} N_i^T N_j \langle 1 - 2\phi_d \phi_f \rangle k_p dV + \int_{\Omega} \mathbf{B}_i^T \mathbf{B}_j dV - \int_{\Omega} \mathbf{B}_i^T \left(\frac{\bar{V}_H}{RT} \nabla \sigma_h \right) N_j dV \quad (79)$$

The resulting finite element system is solved using time parametrisation and an incremental-iterative Newton-Raphson scheme. The implementation is carried out in the commercial finite element package ABAQUS by means of a user element (UEL) subroutine. Abaqus2Matlab (Papazafeiropoulos et al., 2017) is used for pre-processing the input files. Following Martínez-Pañeda et al. (2018), $\nabla\sigma_h$ is computed utilising the derivatives of the shape functions and the hydrostatic stress values at the integration points.

4. Results

By means of several case studies of particular interest, we proceed to showcase the potential of the model in predicting SCC driven by dissolution mechanisms, hydrogen embrittlement or a combination of both. Firstly, we simulate the growth of a semi-circular pit (Section 4.1) and the failure of an embrittled notched plate (Section 4.2), two paradigmatic benchmarks that serve to validate the model. Secondly, we investigate the SCC failures of stainless steel samples under pure bending, considering the role of the passivation film in preventing hydrogen uptake and the transition from anodic-driven SCC to hydrogen-driven SCC (Section 4.3). Thirdly, in Section 4.4, cracking thresholds are predicted for a wide range of environments, spanning the regimes of dominance of hydrogen embrittlement and anodic dissolution, as well as the transition between them. Numerical results are compared with experimental measurements in artificial and biologically-active seawater. Finally, we model the seminal experiments by Gruhl (1984) in Section 4.5 to gain insight into the competition between hydrogen embrittlement and anodic dissolution damage mechanisms.

4.1. Growth of a semi-circular pit

We shall begin by validating model predictions under pure corrosion conditions. Specifically, we simulate pitting corrosion in the absence of mechanical forces. As it has been shown experimentally (Ernst and Newman, 2002), a single growing pit will maintain a semi-circular shape throughout the whole corrosion process if corrosion is diffusion-controlled and only a small region in the edge of the metal is exposed to the electrolyte. To numerically reproduce these observations, we consider a $0.250\text{ mm} \times 0.125\text{ mm}$ rectangular domain with a small semi-circular opening of radius 0.008 mm . The geometric setup, dimensions and boundary conditions are detailed in Fig. 2a. The material and corrosion parameters employed are listed in Table 2.

These are chosen to mimic previous computational studies of this boundary value problem, using either the level set method (Duddu, 2014) or phase field formulations (Mai et al., 2016; Gao et al., 2020). A sufficiently large magnitude of $L \equiv L_0$ is adopted to ensure diffusion-controlled corrosion conditions. In this case study, pitting corrosion occurs in isolation from other phenomena and thus no mechanical load, hydrogen transport or mechanical damage are considered. As shown in Fig. 2b, the finite element mesh is refined in the expected corrosion region. The characteristic element size is 0.001 mm, five times smaller than the interface thickness ℓ_d , and approximately 25,000 plane strain quadratic quadrilateral elements are used.

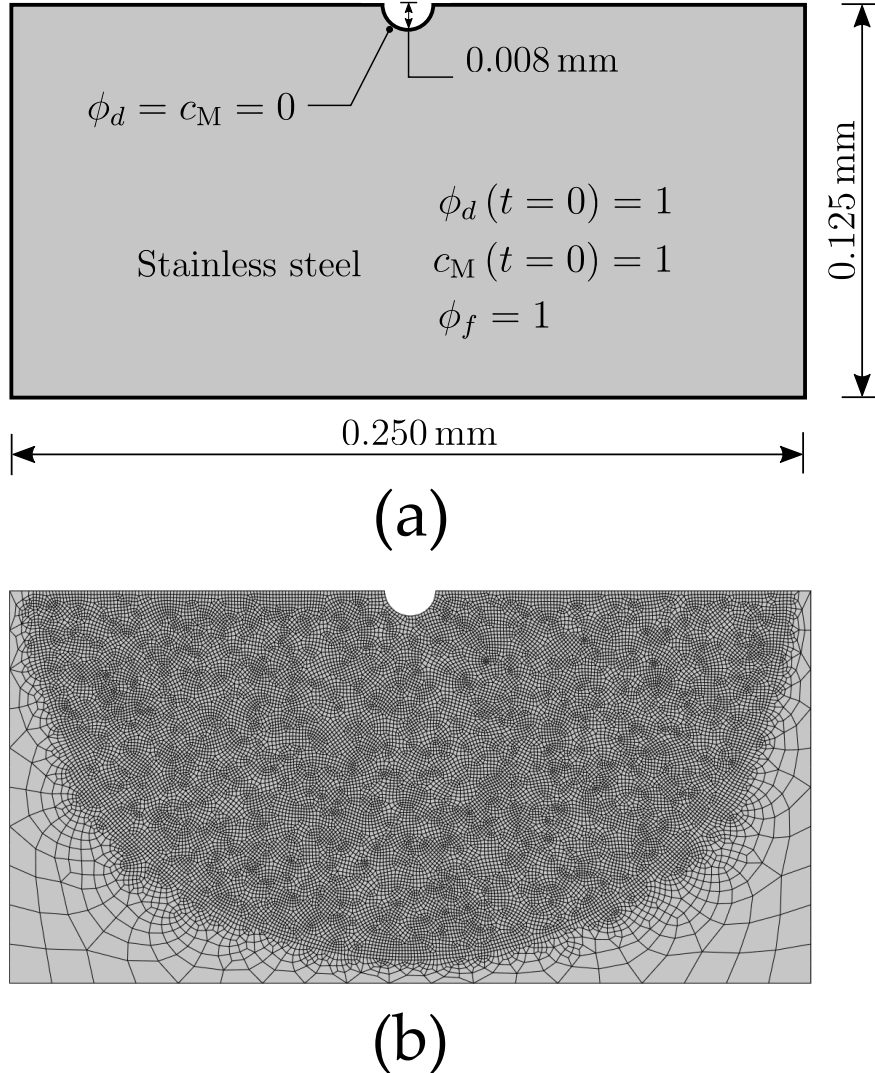


Figure 2: Growth of a semi-circular pit: (a) geometric setup, with the initial and boundary conditions, and (b) finite element mesh.

The results obtained are shown in Fig. 3. The evolution of the corrosion front is captured by

means of the equivalent phases field ϕ_e , which is equal to the dissolution phase field in this case study. In agreement with experiments and previous theoretical studies, the pit grows uniformly with time (see Fig. 3a), with the pit depth versus time exhibiting a parabolic trend typical of diffusion-controlled corrosion (see Fig. 3b). An excellent agreement is attained with the results by Mai et al. (2016), validating the pitting corrosion predictive capabilities of our model and the numerical implementation. The contours of c_M (not shown) mimic those of ϕ_e , indicating that the diffusion of metal ions occurs only on the interface and in the electrolyte, in agreement with expectations - see (T.3).

Table 2: Electrochemical parameters for the semi-circular pitting growth test.

Parameter	Value	Unit
Interface energy γ	10	J/m ²
Interface thickness ℓ_d	0.005	mm
Temperature T	300	K
Diffusion coefficient of metal ion D_M	8.5×10^{-4}	mm ² /s
Interface kinetics coefficient L_0	2×10^6	mm ² /(N · s)
Free energy density curvature A	53.5	N/mm ²
Average concentration of metal c_{solid}	143	mol/L
Average saturation concentration c_{sat}	5.1	mol/L

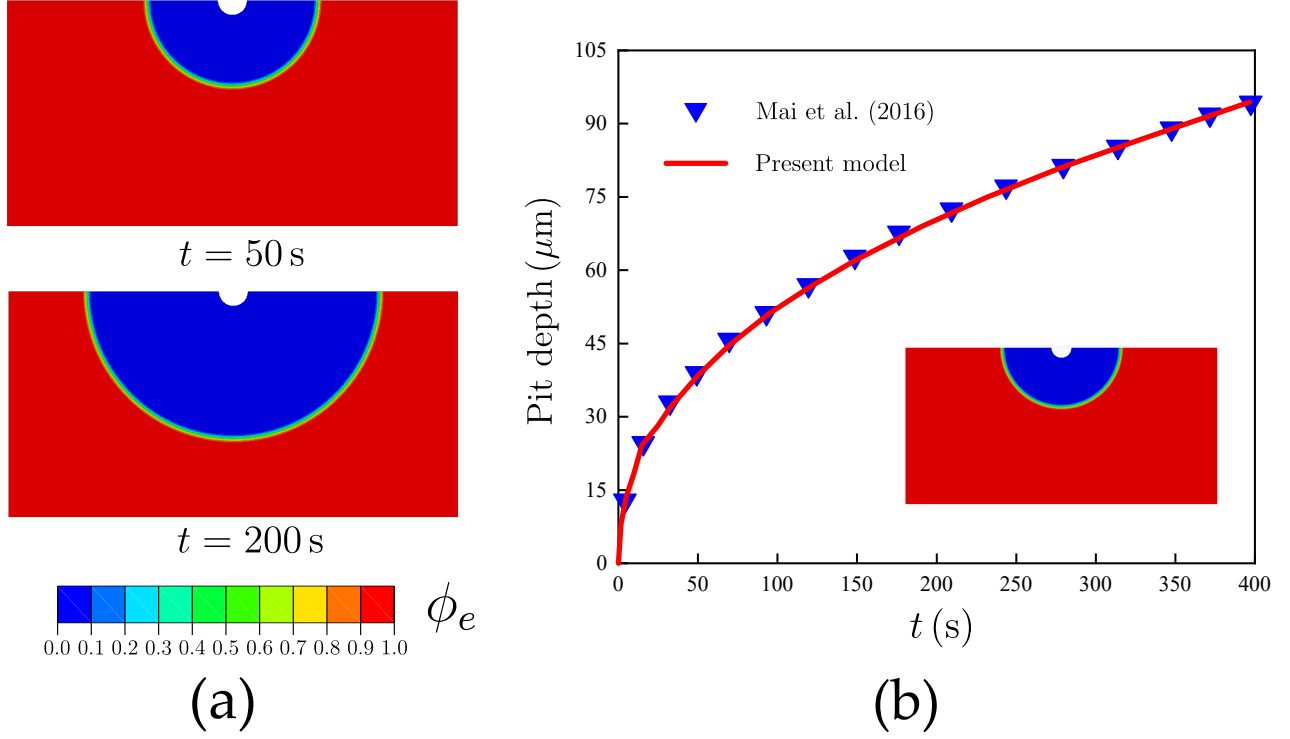


Figure 3: Growth of a semi-circular pit: (a) contours of the damage variable ϕ_e , and (b) predictions of pit depth versus time, including the results by Mai et al. (2016).

Now, we extend this case study to investigate the role of the passive film. Thus, in addition to the case of $k = 0$ (no film), shown in Fig. 3, we consider the presence of a passivation film with different degrees of stability and protection, as characterised by selected values of k (namely, 0.1, 0.2, 0.5 and 1). The time interval t_0 in (44) is chosen to be 0, implying that the film starts protecting the surface from its creation. Also, we emphasise that no mechanical loading is applied in this study, so the film never ruptures and just increases its protective capabilities with time. The results obtained are shown in Fig. 4, in terms of pit depth versus time. It can be seen that, initially, the pit grows at approximately the same rate for all cases, independently of the stability of the film. This is because the film reduces corrosion kinetics progressively and pitting is initially occurring at high current densities (high L_0 , diffusion-controlled corrosion). As the corrosion time increases, the cases with $k > 0$ show how corrosion changes from diffusion-controlled to activation-controlled as L decreases, up to the point where passivation prevents the material from corroding entirely. These results showcase the capabilities of the model in incorporating the role of film passivation in corrosion predictions.

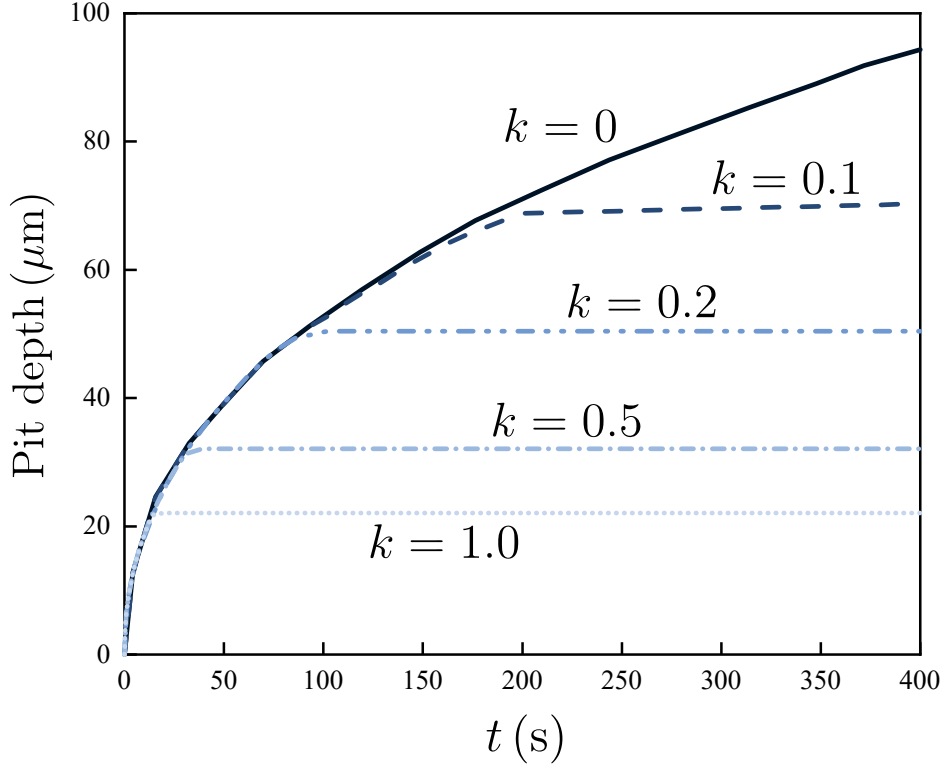


Figure 4: Growth of a semi-circular pit: Pit growth as a function of corrosion time for five selected values of the film stability parameter k .

4.2. Hydrogen assisted cracking of a notched square plate

Insight and verification of the abilities of the model in predicting hydrogen embrittlement and cracking are attained by simulating the fracture of a notched square plate in a hydrogenous environment; a paradigmatic benchmark in the phase field fracture and phase field hydrogen embrittlement communities (Miehe et al., 2010; Martínez-Pañeda et al., 2018; Mandal et al., 2021). As shown in Fig. 5a, we consider a $1 \text{ mm} \times 1 \text{ mm}$ rectangular domain with a straight horizontal notch of length 0.5 mm at the mid-height of the left edge. The bottom edge is fixed and a vertical displacement is applied to the top edge. No corrosion effects are considered ($\phi_e = \phi_f$) and the relevant material properties are listed in Table 3. Again, material parameters are chosen in agreement with previous computational studies (Miehe et al., 2010; Martínez-Pañeda et al., 2018). The chemical initial and boundary conditions are as follows. First, the plate is uniformly charged with hydrogen such that $c_H(t = 0) = c_{\text{env}} \forall \mathbf{x}$. Also, during the experiment, we enforce the penalty boundary condition such that $c_H = c_{\text{env}}$ in the cracked regions. Selected values of c_{env} are chosen to visualise the impact of increasing hydrogen content on fracture resistance; namely,

0 (no hydrogen), 0.1, 0.5 and 1 wt ppm. The mesh is refined in the expected crack propagation area, ensuring that the length scale parameter ℓ_f is at least 5 times larger than the characteristic element size (see Fig. 5b). Approximately 30,000 plane strain quadratic quadrilateral elements are used to discretise the plate.

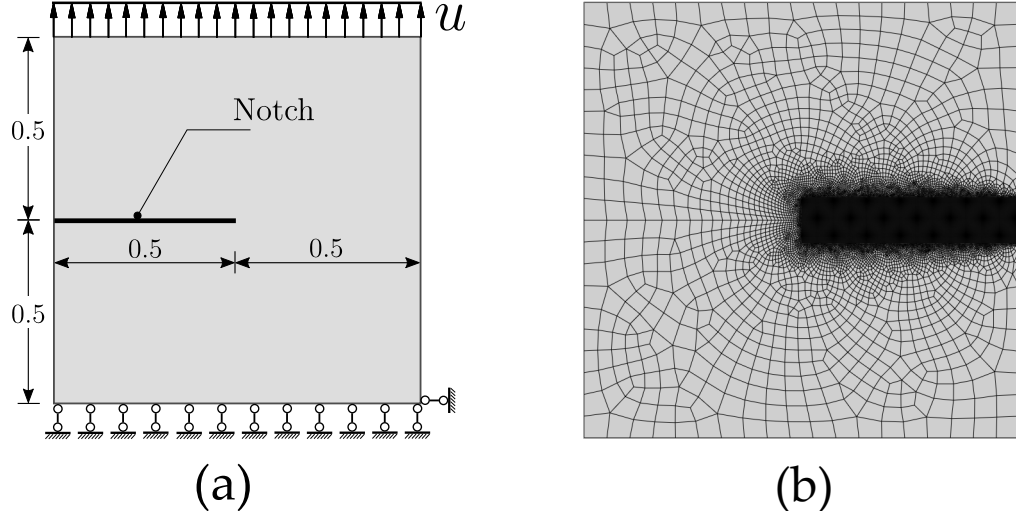


Figure 5: Hydrogen assisted cracking of a notched square plate: (a) geometry and mechanical loading, and (b) finite element mesh.

Table 3: Hydrogen assisted cracking of a notched square plate: material properties (Miehe et al., 2010; Martínez-Pañeda et al., 2018).

Parameter	Value	Unit
Young's modulus E	210,000	MPa
Poisson's ratio ν	0.3	—
Critical energy release rate $G_c(0)$	2.7	kJ/m ²
Length scale parameter ℓ_f	0.0075	mm
Hydrogen diffusion coefficient D_H	0.0127	mm ² /s
Trap binding energy Δg_b^0	30	kJ/mol
Partial molar volume \bar{V}_H	2000	mm ³ /mol
Hydrogen damage coefficient χ	0.89	—

The force versus displacement curves obtained are shown in Fig. 6. In the absence of hydrogen ($c_{\text{env}} = 0$), predictions agree very well with the results by Miehe et al. (2010), validating

the phase field fracture implementation. As the concentration of hydrogen increases, we observe a significant drop in the load carrying capacity of the plate, with crack growth initiating earlier and a notable reduction in the critical load. This is due to the hydrogen-induced degradation of the material toughness - see (T.4). Qualitatively, the results obtained agree with those reported in the literature. However, quantitative differences can be observed because, unlike in Martínez-Pañeda et al. (2018), the damaged hydrostatic stress is used to drive hydrogen diffusion, see (T.5). Representative contours of the damage variable ϕ_e and hydrogen concentration c_H are shown in Fig. 7, for a given moment in time. In agreement with expectations, $c_H = c_{\text{env}}$ at the crack tip (as dictated by the *moving* chemical boundary condition), and a higher hydrogen content is seen immediately ahead of the crack tip, where hydrostatic stresses are large. Thus, the present results validate the phase field fracture implementation and show that the interplay between hydrogen diffusion, fracture and mechanical deformation is adequately captured.

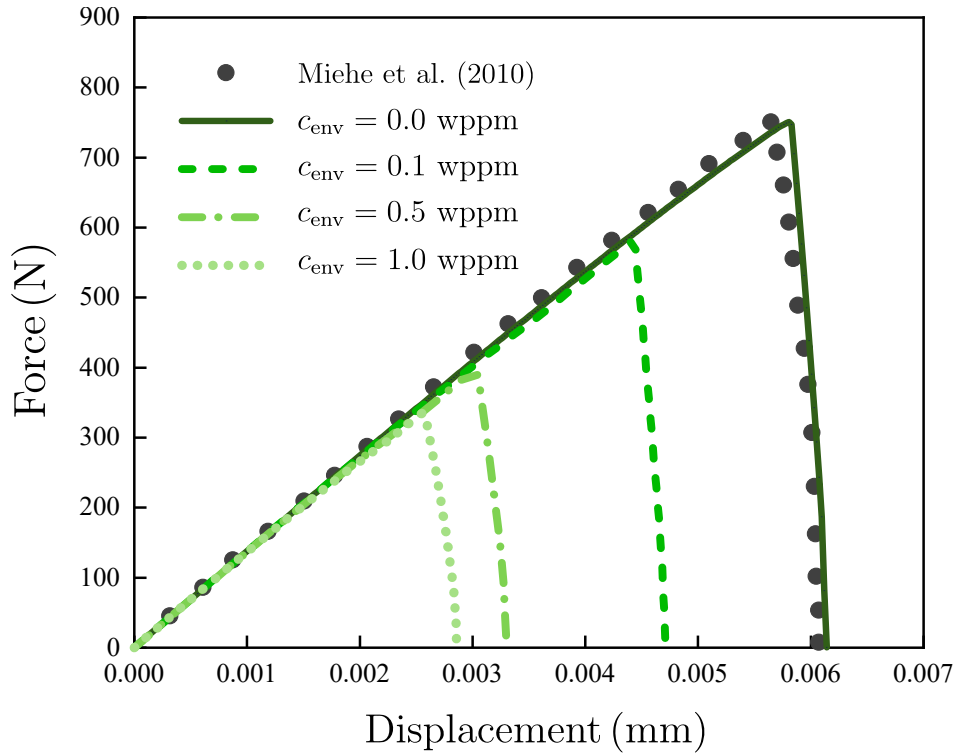


Figure 6: Hydrogen assisted cracking of a notched square plate: Force versus displacement curves for different hydrogen contents. The case without hydrogen ($c_{\text{env}} = 0$) matches the results by Miehe et al. (2010).

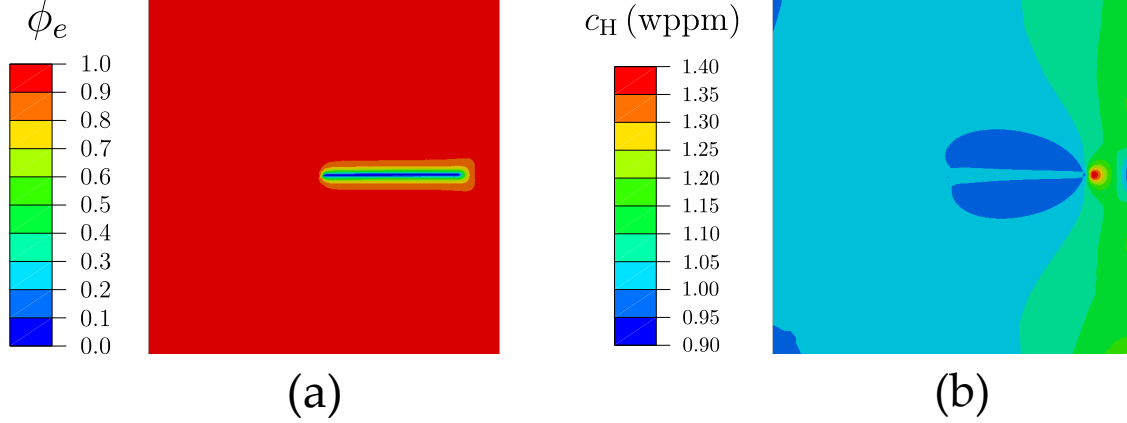


Figure 7: Hydrogen assisted cracking of a notched square plate: Contours of (a) damage variable ϕ_e and (b) hydrogen concentration c_H , when $c_{\text{env}} = 1.0$ wppm and the remote displacement equals $u = 0.0028$ mm.

4.3. Bending of stainless steel samples: transition from anodic dissolution to hydrogen embrittlement

We proceed to investigate the transition between anodic dissolution and hydrogen assisted damage mechanisms, as well as their interactions. For this purpose, we simulate the failure of a stainless steel beam of dimensions $10 \text{ mm} \times 2 \text{ mm}$ undergoing pure bending while exposed to a corrosive environment. Taking advantage of symmetry, only half of the beam is modelled, as shown in Fig. 8, where the geometry, initial and boundary conditions are given. The beam height equals $H = 2 \text{ mm}$ while the half-beam length is $W/2 = 5 \text{ mm}$. The mechanical boundary condition corresponds to an applied curvature κ_{app} , such that the horizontal displacement at the beam ends evolves as,

$$u_x = x_1 x_2 \kappa_{\text{app}} \quad \text{at} \quad x_1 \pm W/2 \quad (80)$$

Here, we choose to apply an initial curvature at $t = 0$ and then increase its magnitude with time; namely: $\kappa_{\text{app}} = 0.001 + 2 \times 10^{-8} t$. Similar to Section 4.1, we assume that the stainless steel is well-protected from the corrosive environment except for a small semi-circular pit of radius 0.1 mm , located at the centre of the top free surface and where the Dirichlet boundary conditions $\phi_d = 0$, $c_M = 0$ and $c_H = c_{\text{env}} = 1 \text{ wppm}$ are prescribed. The dissolution phase field length scale is chosen to be $\ell_d = 0.06 \text{ mm}$ (Mai and Soghrati, 2017), while the mobility parameter equals $L_0 = 1 \times 10^{-5} \text{ mm}^2/(\text{N} \cdot \text{s})$, to ensure activation-controlled corrosion conditions. The remaining electrochemical parameters are those reported in Table 2. The hydrogen diffusion coefficient is defined as $D_H = 5.8 \times 10^{-6} \text{ mm}^2/\text{s}$, as reported in Luo et al. (2021). In regard to the mechanical

properties, the constitutive behaviour is characterised by a Young modulus of $E = 190$ GPa, a Poisson's ratio of $\nu = 0.3$, a yield stress of $\sigma_y = 400$ MPa, and a strain hardening exponent of $N = 0.1$ (Chen and Young, 2006). The fracture toughness is assumed to be $G_c(0) = 1.2$ kJ/m². We adopt a material strength of $\sigma_c = 800$ MPa which, according to (60), renders a phase field fracture length scale of $\ell_f = 0.04$ mm. All the other parameters correspond to those listed in Table 3.

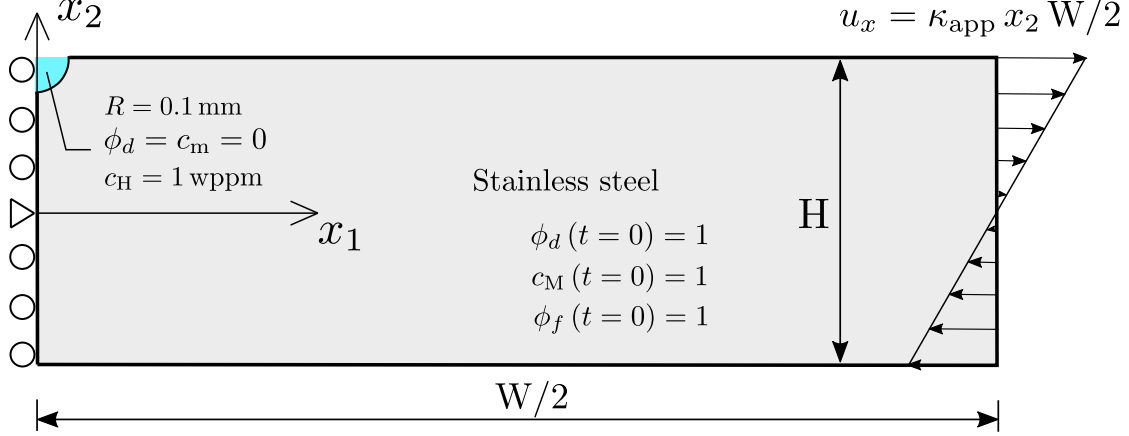


Figure 8: Bending of stainless steel samples: schematic with the configuration, dimensions and initial and boundary conditions.

A passivation film deposits on the surface of the stainless steel sample and is ruptured if the local strain level is sufficiently high. This is captured by the film-rupture-dissolution-repassivation (FRDR) formulation presented in Section 2.5.2. The interplay between film rupture and the environment is characterised by the parameters $k = 0.0001$, $t_0 = 50$ s, and $\varepsilon_f = 0.003$. Moreover, it is well-known that the presence of a passive film can prevent the uptake of hydrogen (see, e.g., Schomberg and Grabke, 1996). We incorporate this film-hydrogen interaction by defining, when the passive film begins to stabilise ($t_i > t_0$), a sufficiently low hydrogen diffusion coefficient D_H along the electrolyte-metal interface ($\phi_d \leq 0.95$); i.e.,

$$\begin{cases} D_H \rightarrow 0, & \text{if } t_i > t_0 \text{ and } \phi_d \leq 0.95 \\ D_H \equiv D_H, & \text{otherwise} \end{cases} \quad (81)$$

For numerical reasons, D_H is not chosen to be exactly zero but equal to a small value. Specifically, a magnitude of $D_H = 1 \times 10^{-10}$ mm²/s achieves the desired effect. One should note that the uptake of hydrogen is only hindered at the interface; the formulation still captures the condition

$c_H \equiv c_{\text{env}}$ in all regions of the evolving electrolyte due to the penalty boundary condition (74). A total of approximately 13,000 quadrilateral quadratic elements with reduced integration are used to discretise the model, with the mesh being particularly refined in the expected SCC region.

Numerical experiments are conducted to investigate the influence of the various parameters at play. First, we compare the predictions obtained with and without the film-hydrogen interaction defined in (81). The results are shown in Fig. 9 for two instants of time, $t = 5$ and $t = 9$ hours. It can be observed that for short time scales ($t \leq 5$ h), predictions are relatively similar, suggesting that SCC growth is dominated by anodic dissolution. However, when there is enough time for hydrogen to ingress and diffuse in the sample, then differences become significant. The length of the SCC crack is twice as large if the model does not account for the interplay between hydrogen uptake and film passivation.

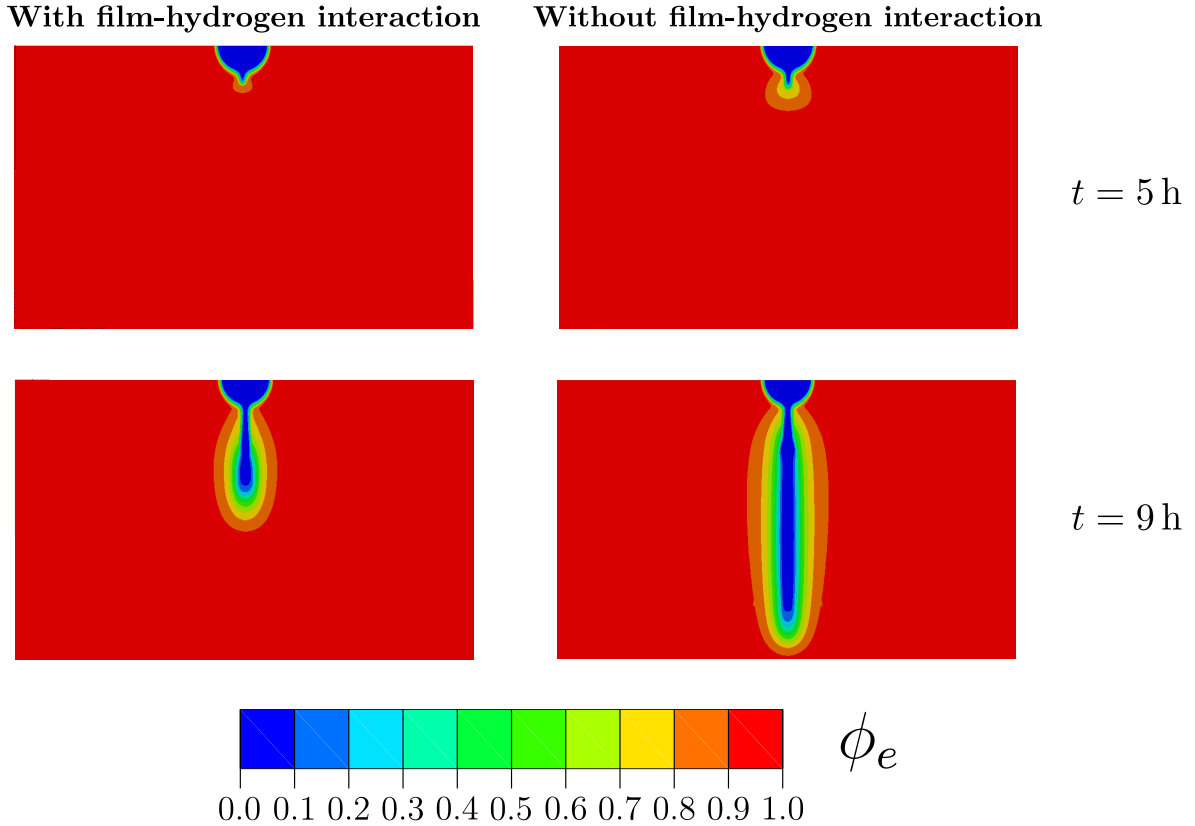


Figure 9: Bending of stainless steel samples: predictions of the evolution of the SCC damage region considering and neglecting the interaction between hydrogen uptake and film passivation.

Further insight into this film-hydrogen uptake interplay is gained by plotting the normalised

distribution of hydrogen content, see Fig. 10. The SCC defect length at each reported time period can be readily identified from the hydrogen distribution plots, as it is associated with a drop in c_H from c_{env} . Thus, it can be seen that the SCC defect lengths predicted by models with and without the film-hydrogen interaction condition (81) are very close for $t = 5$ h, but significant differences are observed after 9 h. This is due to the shift in damage driving force mechanism. For $t \leq 5$ h, the growth of the SCC defect is driven by anodic dissolution. However, as time increases, two effects become relevant. First, the SCC defect sharpens due to the role of the mechanics-enhanced corrosion terms (44) and this is further enhanced as a result of the localised rupture of the passive film. Second, the applied load increases with time. These two features lead to a localised stress raise, which increases the hydrogen content (57) and the energy release rate. This triggers a shift between anodic dissolution- and hydrogen embrittlement-driven SCC defect growth. Additionally, the results in Fig. 10 show how the condition (81) influences hydrogen uptake, with a sharp drop in the hydrogen content being observed for the cases in which the passivation layer impedes hydrogen ingress. However, one should note that hydrogen ingress still takes place to a certain extent, as there is a time t_0 in each repassivation-rupture cycle where the film has not had enough time to stabilise and protect.

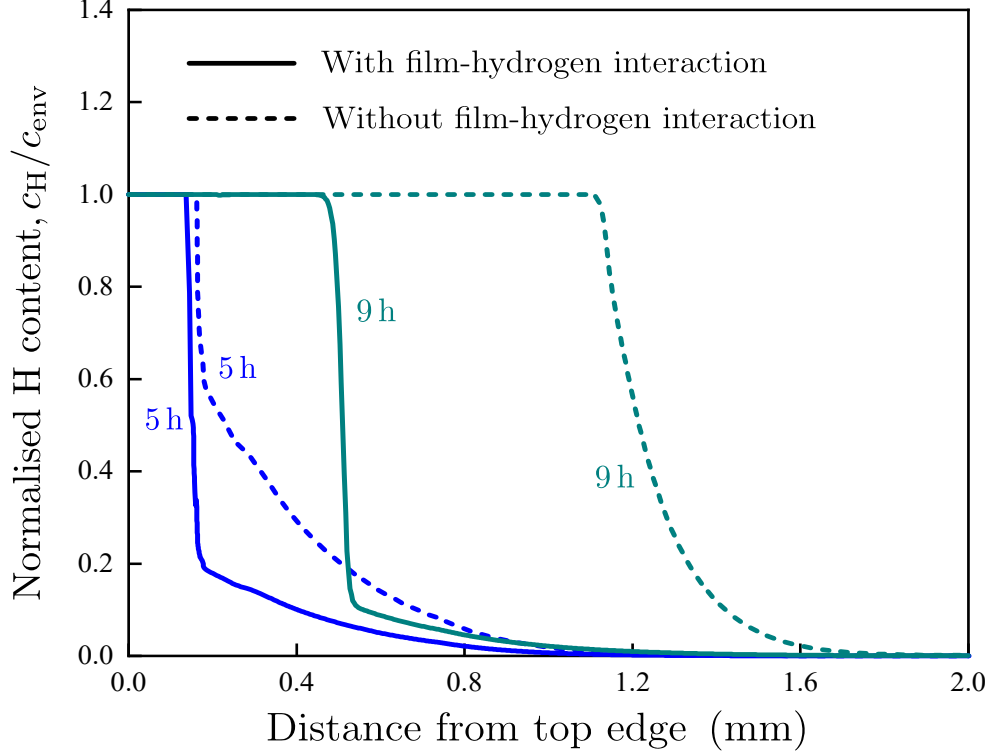


Figure 10: Bending of stainless steel samples: normalised hydrogen content along the extended SCC propagation path as predicted considering and neglecting the interaction between hydrogen uptake and film passivation.

We conclude this case study by investigating how the film rupture resistance influences the transition from anodic dissolution to hydrogen embrittlement SCC defect growth. For this purpose, it is assumed that SCC defect growth is dominated by hydrogen embrittlement mechanisms if $\phi_f \leq 0.05$. The results obtained are reported in Fig. 11 in terms of the length of the SCC region versus time, with a cross being used to highlight the transition point from anodic dissolution dominance to hydrogen embrittlement dominance. Four curves are shown, each for a different film failure strain ε_f . In all cases, the role of the passivation film in preventing hydrogen uptake is accounted for; as elaborated above, this hinders hydrogen ingress but does not completely preclude it, due to the time required for the film to stabilise. In agreement with expectations, the results reveal that the SCC defect grows faster if the fracture resistance of the film is smaller. The rate of SCC defect growth increases with time due to the sharpening of the SCC pit - the tip of the defect acts as a stress concentrator, which favours a very localised rupture of the film and increases dissolution rates in regions of high stresses and strains. Defect growth rates are further augmented when hydrogen mechanisms dominate stress corrosion cracking, with the crack

eventually propagating in an unstable manner. The interplay between ε_f and the transition to hydrogen embrittlement is more complex. The sensitivity of the transition time to ε_f agrees with expectations; hydrogen embrittlement becomes dominant later in time for larger values of ε_f , as these lead to smaller hydrogen exposure times and lower SCC growth rates overall. However, ε_f has a dual influence on the length of the SCC defect at which hydrogen embrittlement dominance is attained. On the one hand, longer times lead to higher values of the energy release rate, favouring hydrogen-assisted mechanical cracking relative to dissolution-driven defect growth. On the other hand, the higher ε_f values associated with larger failure times result in a reduced environmental exposure and thus a smaller size of the hydrogen-degraded region.

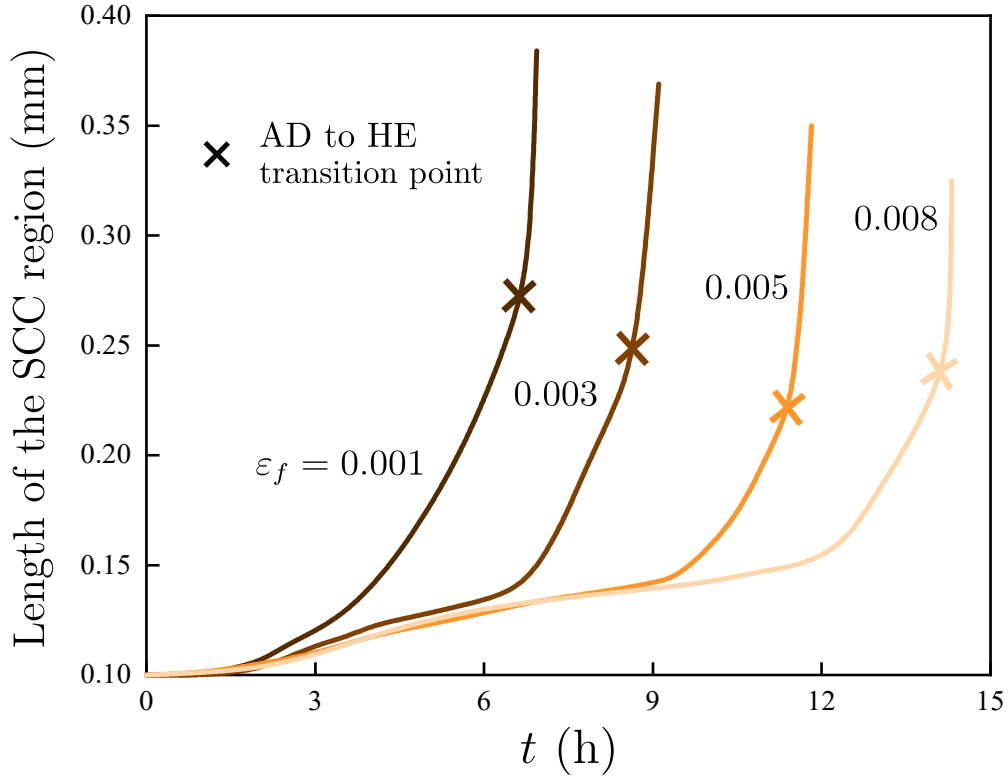


Figure 11: Bending of stainless steel samples: Length of the SCC region as a function of time for four representative failure strain values. A cross is used to denote the time at which the growth of the SCC defect transitions from being driven by anodic dissolution to being dominated by hydrogen embrittlement mechanisms ($\phi_f \leq 0.05$).

4.4. SCC threshold predictions in artificial and biologically-active seawater

The experiments by Robinson and Kilgallon (1994) on heat-treated steel 690 are simulated and extended to illustrate the ability of the model to predict cracking thresholds under the dominance of anodic dissolution or hydrogen embrittlement mechanisms, as well as in the transition

from one to the other. Steel 690 samples were exposed to sterile artificial seawater (SAS) and biologically active seawater (BAS); the existence of bacteria in BAS increases sulfide concentration and consequently promotes hydrogen uptake. Experiments were conducted at a wide range of cathodic protection potentials and stress intensity thresholds K_{th} were measured in each scenario. As sketched in Fig. 12a, the experiments were conducted using a double-cantilever beam (DCB) configuration with an initial crack. Given that small scale yielding conditions prevail, we simplify the loading configuration by using a so-called boundary layer model, where a remote K_I -field is prescribed, characterising the stress state near the crack in the DCB test (see Fig. 12b). Thus, the loading conditions are defined by simulating a semi-circular geometry and prescribing the displacements on the outer surface in agreement with Williams (1957) elastic solution; i.e., the horizontal and vertical displacements of the outer nodes respectively read,

$$u_x = K_I \frac{1+\nu}{E} \sqrt{\frac{r}{2\pi}} (3 - 4\nu - \cos \theta) \cos \left(\frac{\theta}{2} \right) \quad (82)$$

$$u_y = K_I \frac{1+\nu}{E} \sqrt{\frac{r}{2\pi}} (3 - 4\nu - \cos \theta) \sin \left(\frac{\theta}{2} \right) \quad (83)$$

where r and θ are the coordinates of a polar coordinate system centred at the crack tip.

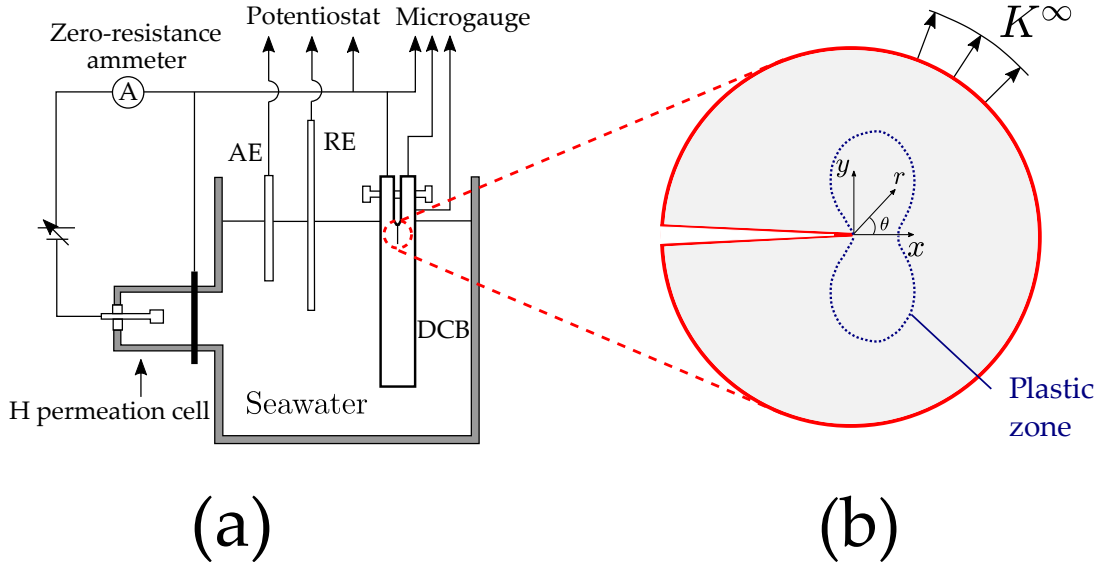


Figure 12: SCC threshold predictions as a function of the environment: Schematic illustration of (a) the DCB test configuration (Robinson and Kilgallon, 1994), and (b) the boundary layer model to reproduce crack tip loading conditions under the assumption of small scale yielding.

The electrochemical parameters listed in Table 2 are adopted unless otherwise stated. A phase field corrosion length scale of $\ell_d = 0.05$ mm is used. According to Tian et al. (2018), no

passivation occurs in low-alloy steels across a wide range of artificial seawater environments, such that $k = 0$ in (44) is considered throughout this analysis. The constitutive parameters for steel 690 are determined as $E = 210$ GPa, $\nu = 0.3$, and $N = 0.1$ based on the uniaxial stress-strain data reported by Billingham et al. (2003), while the yield strength is taken to be $\sigma_y = 1032$ MPa, as reported by Robinson and Kilgallon (1994). In the absence of hydrogen, we consider a material toughness of $G_c(0) = 10$ kJ/m², which is estimated from the stress intensity threshold measured in an inert environment (Robinson and Kilgallon, 1994). The phase field length scale can be chosen in agreement with (60), for known values of E , G_c and the material strength σ_c . No data for σ_c is available but given the low hardening of these alloys, the ultimate tensile strength is expected to be between σ_y and 1.5 times σ_y . These would give ℓ_f values of 0.09 and 0.21 mm; accordingly we choose the intermediate value $\ell_f = 0.15$ mm. Mimicking the experiments, a very slow load rate is considered, $\dot{K}_I = 10^{-5}$ MPa $\sqrt{\text{m}}$ /s, such that there is sufficient time for the hydrogen to achieve steady state conditions. Robinson and Kilgallon (1994) report K_{th} versus hydrogen content curves, as the focus was on cathodic protection conditions, where hydrogen embrittlement is dominant. The cathodic potential is applied from -0.85 V to -1.25 V with an interval of 0.1 V, such that a total of ten stress intensity thresholds are recorded with different hydrogen concentrations. We will extend the range of applied potentials beyond the experiments to predict the transition to dissolution-driven SCC, but begin by reproducing the testing data for hydrogen embrittlement conditions. For the low applied potentials of the experimental campaign, material dissolution is likely to be negligible and accordingly a very small interface kinetics coefficient of $L_0 = 10^{-15}$ mm²/(N · s) is considered, with $\phi_d = c_M = 0$ defined as initial conditions at the crack tip node. The hydrogen initial and boundary conditions involve the definition of an initial uniform hydrogen concentration throughout the sample $c_H(t = 0) = c_{\text{env}} \forall \mathbf{x}$, and the application of the boundary condition $c_H = c_{\text{env}}$ in the crack surfaces. A diffusion coefficient of $D_H = 2 \times 10^{-6}$ mm²/s is defined, as reported by Robinson and Kilgallon (1994). The mesh in the vicinity of the crack is refined to be at least 10 times smaller than both the interface thickness ℓ_d and the length scale parameter ℓ_f , so as to ensure the mesh insensitive results. Only half of the boundary layer model is considered, taking advantage of symmetry, and the model is discretised with approximately 65,000 quadratic quadrilateral elements with reduced integration.

Experimental and computational predictions of stress intensity threshold K_{th} versus hydrogen

content are shown in Fig. 13. The numerical results have been obtained considering two hydrogen degradation laws: (i) the atomistically-informed one presented in Section 2.4.4, with $\chi = 0.98$, and (ii) a phenomenological degradation law that provides a good fit to the experiments. The latter is given by the following higher order function:

$$G_c(\theta) = (0.0285\theta^4 - 0.3532\theta^3 + 1.433\theta^2 - 2.0934\theta + 1) G_c(0) \quad (84)$$

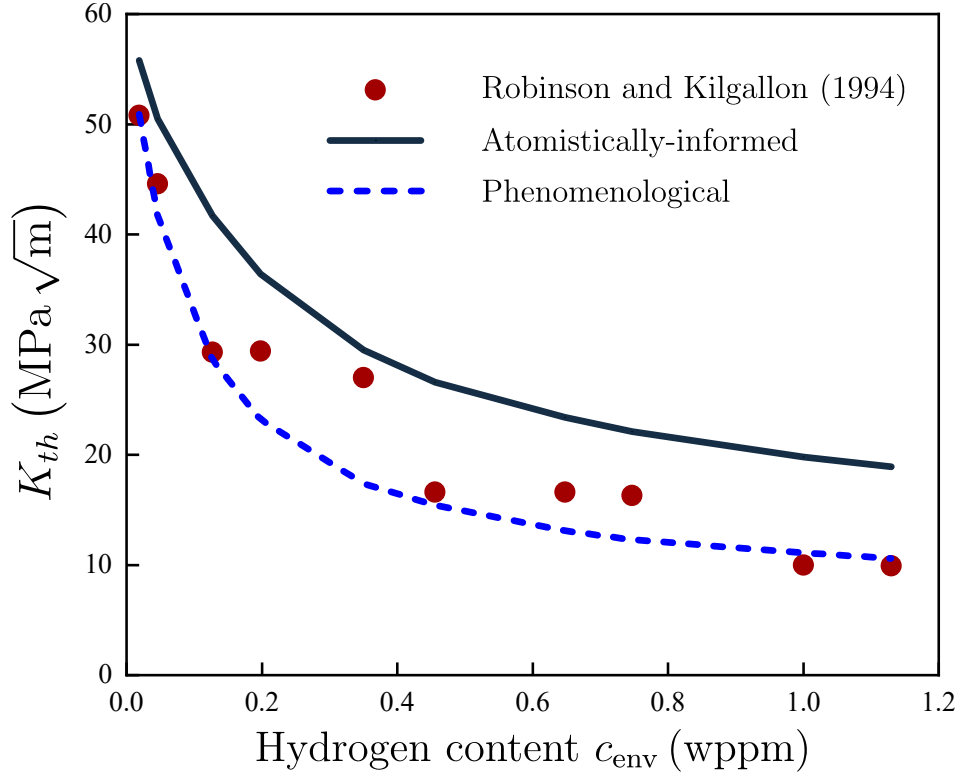


Figure 13: SCC threshold predictions as a function of the environment: experimental (Robinson and Kilgallon, 1994) and modelling predictions of K_{th} versus hydrogen concentration c_{env} . The numerical results have been obtained with an atomistically-inspired hydrogen degradation law, Eq. (31), and with a phenomenological one, Eq. (84).

Both degradation laws lead to the same qualitative outcome: a significant reduction in K_{th} with increasing hydrogen content. However, the atomistically-informed one slightly underpredicts the degree of embrittlement, independently of the choice of χ (the hydrogen damage coefficient). The sensitivity of the material toughness as a function of the hydrogen concentration is shown in Fig. 14. It can be seen that the atomistic relation saturates as $\chi \rightarrow 1$ at higher levels of G_c , relative to the degradation law derived from experiments. However, the first principles

predictions are very sensitive to the choice of the interface binding energy - see Eq. (30). Here, a value of 30 kJ/mol has been chosen based on an average of the experimental data available for grain boundaries but measurements can range from 17 to 59 kJ/mol (Asaoka et al., 1977; Choo and Lee, 1982). Reducing the uncertainty in the characterisation of trap binding energies is arguably the bottleneck for parameter-free mechanistic modelling of hydrogen assisted cracking.

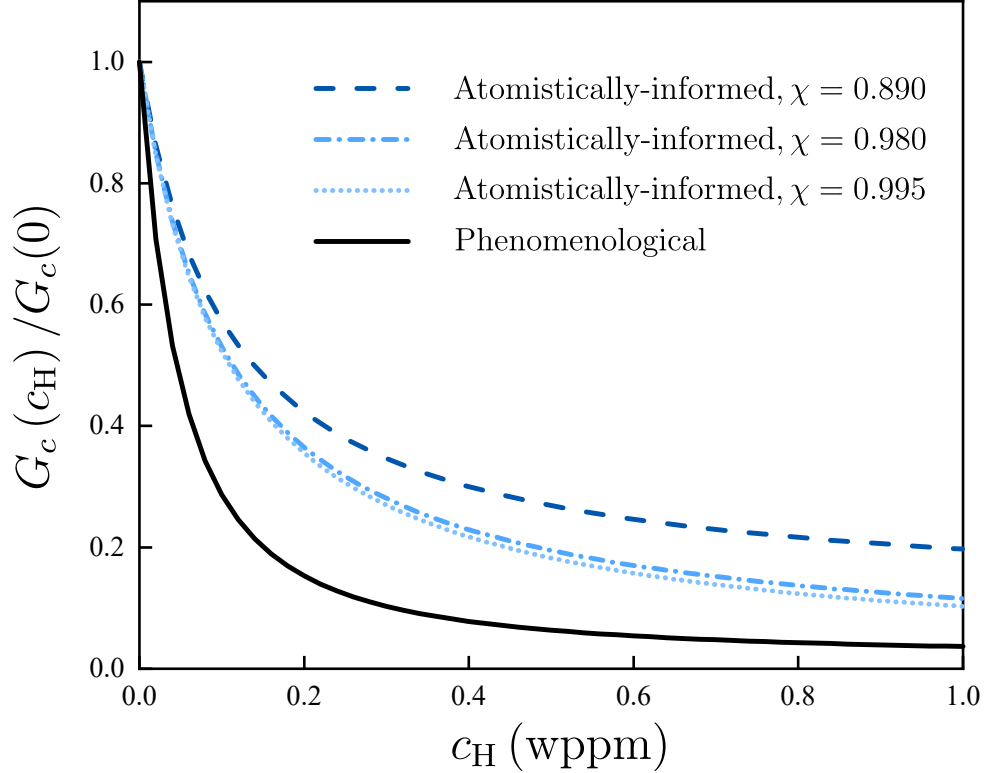


Figure 14: SCC threshold predictions as a function of the environment: Sensitivity of the material toughness to the hydrogen content, as predicted by both the atomistically-informed degradation law (31) and by the phenomenological relation (84). The atomistic approach uses an interface binding energy of 30 kJ/mol.

Now, let us model a wider range of environments, as characterised by the applied potential E_p , to additionally consider conditions of free corrosion and anodic-driven SCC. The polarisation curves reported by Tian et al. (2018) for similar conditions (material, solutions) will be used to determine the free corrosion potential E_{corr} , and a higher E_p , such that anodic dissolution becomes the dominant mechanism for cracking. To capture the sensitivity to the applied potential, we will exploit the relation between the interface mobility parameter L and the corrosion current density i , as elaborated next. Let us assume a stress-free condition, leaving aside the dependency of the mobility coefficient on mechanical fields (i.e., $L \equiv L_0$). Also, let us assume activation-

controlled corrosion conditions (i.e., a sufficiently small $L \equiv L_0$). Under activation-controlled conditions, the corrosion velocity v_n is related to the current density i through Faraday's second law for electrolysis:

$$v_n = \frac{i}{zF c_{\text{solid}}} \quad (85)$$

where $z = 2.1$ is the average charge number and F is Faraday's constant. Recall now the Allen-Cahn type equation used to evolve the corrosion phase field, (T.2). Since, in activation-controlled corrosion, $v_n \equiv d\phi_d/dt$, the combination of (85) and (T.2) implies that the interface mobility coefficient is proportional to the current density: $L \propto i$. It follows immediately that for any corrosion current density (e.g., i_1), the associated mobility coefficient (L_1) can be readily determined, provided that the proportionality constant is known for another current (e.g., L_2/i_2); i.e.,

$$L_1 = i_1 \frac{L_2}{i_2} \quad (86)$$

Accordingly, one can run a uniform corrosion simulation with any sufficiently small L value that leads to activation-controlled corrosion conditions, compute the velocity of the corrosion front v_n and use (85) to estimate the current density associated with that L (Mai et al., 2016). Once the L/i ratio is known, Eq. (86) can be used to obtain the interface mobility coefficient for any given corrosion current density. Accordingly, we use the polarisation data by Tian et al. (2018) and follow this strategy to determine the mobility coefficient associated with the free corrosion current density i_{corr} for two environments, R2 and AS2, that respectively resemble the sterile artificial seawater and biologically active seawater solutions. First, a simulation with a small value of $L = L_0 = 2 \times 10^{-8} \text{ mm}^2/(\text{N} \cdot \text{s})$ is conducted, leading to $v_n = 3.3 \times 10^{-9} \text{ mm/s}$ and, *via* (85), $i = 9.6 \times 10^{-8} \text{ A/mm}^2$ ($L/i = 0.2083$). Now, we use (86) to find a value of $L_{\text{corr}} = L_0 = 3.3 \times 10^{-10} \text{ mm}^2/(\text{N} \cdot \text{s})$, as the mobility coefficient associated with the free corrosion current density i_{corr} for sterile artificial seawater (where $i_{\text{corr}} = 1.59 \times 10^{-9} \text{ A/mm}^2$), and of $L_{\text{corr}} = L_0 = 3.33 \times 10^{-9} \text{ mm}^2/(\text{N} \cdot \text{s})$ for biologically active seawater (where $i_{\text{corr}} = 1.6 \times 10^{-8} \text{ A/mm}^2$). These values correspond to the corrosion potential, which equals $E_{\text{corr}} = -0.74 \text{ V}_{\text{SCE}}$ for sterile artificial seawater and $E_{\text{corr}} = -0.65 \text{ V}_{\text{SCE}}$ for biologically active seawater. A similar but slightly different strategy is used to determine the mobility coefficients associated with the anodic condition. Here, we utilise the corrosion velocity measurements by Tian et al. (2018), use that value to compute i *via* (85) and then determine E_p using their polarisation

curves and the associated mobility coefficient through (86). This leads to values of $E_p = -0.68$ V_{SCE}, $L_0 = 9.2 \times 10^{-8}$ mm²/(N · s) and $E_p = -0.63$ V_{SCE}, $L_0 = 3.1 \times 10^{-7}$ mm²/(N · s) for sterile artificial seawater and biologically-active seawater, respectively. To estimate the hydrogen content across all applied potentials we apply a linear fit to the data provided by Robinson and Kilgallon (1994) and extrapolate.

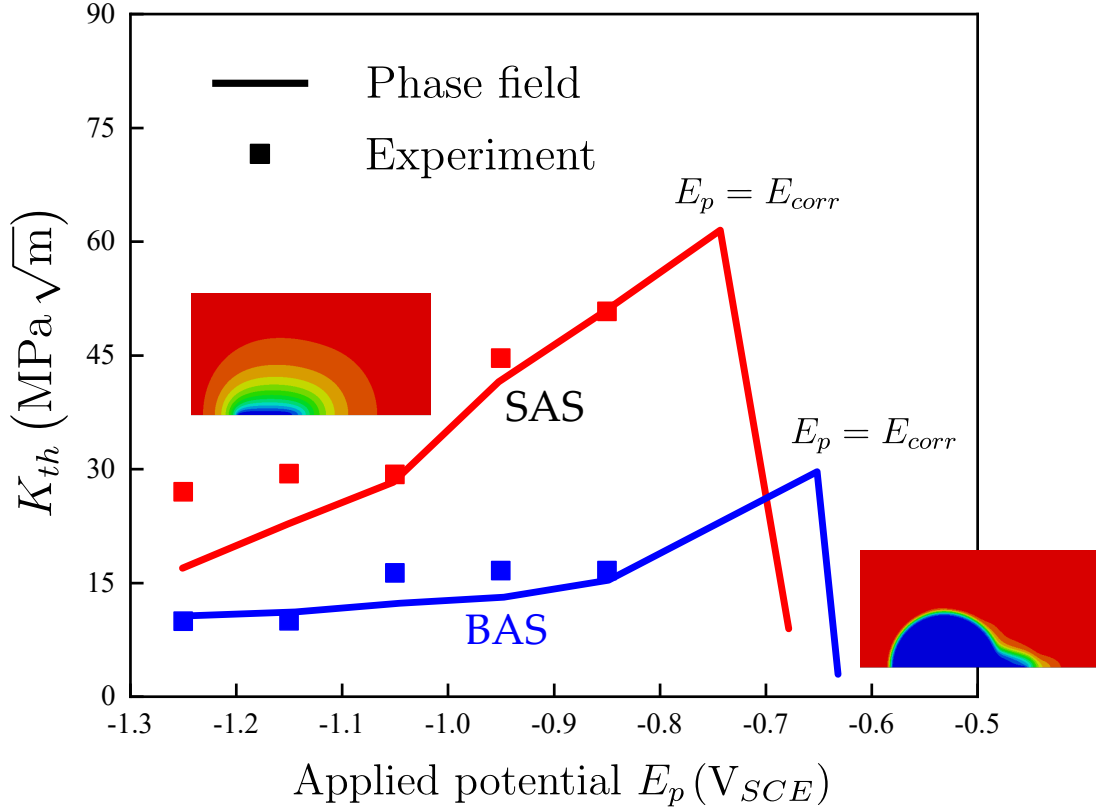


Figure 15: SCC threshold predictions as a function of the environment: Stress intensity threshold K_{th} versus applied potential E_p , for both sterile artificial seawater (SAS) and biologically active seawater (BAS). The cathodic region includes experimental data by Robinson and Kilgallon (1994).

The results obtained are shown in Fig. 15, in terms of cracking thresholds K_{th} versus applied potential E_p , for both sterile artificial seawater (SAS) and biologically active seawater (BAS). The experimental data obtained by Robinson and Kilgallon (1994) for the cathodic region is also shown. The model agrees quantitatively with experiments in the cathodic region and qualitatively captures the expected trends for E_{corr} and higher applied potentials. Namely, K_{th} increases with applied potential until reaching the peak at $E_p = E_{corr}$, and then drops again as the applied potential enters the regime where cracking is driven by anodic SCC mechanisms (Lee and Gangloff, 2007; Pioszak and Gangloff, 2017). Thus, the model can satisfactorily predict the

sensitivity of cracking thresholds to the environment across all regimes: cathodic, corrosion and anodic potentials.

4.5. SCC tube testing of Al alloys (Gruhl, 1984): hydrogen embrittlement vs anodic dissolution

Finally, we gain insight into the competition between anodic dissolution and hydrogen damage mechanisms by modelling the classic Gruhl (1984) experiments on Al alloys. As shown in Fig. 16, Gruhl (1984) shed light into the nature of SCC in Al alloys by conducting tensile tests on cylindrical samples that were exposed to a corrosive environment on their inner surface and had a notch in the outer one. If stress corrosion cracking was driven by anodic mechanisms, then cracks should initiate from the inner surface. However, if SCC failures were governed by hydrogen embrittlement, then cracking should initiate close to the notch, in a region far from the corrosive medium but where hydrogen could diffuse and accumulate due to the role that the notch plays as a stress concentrator.

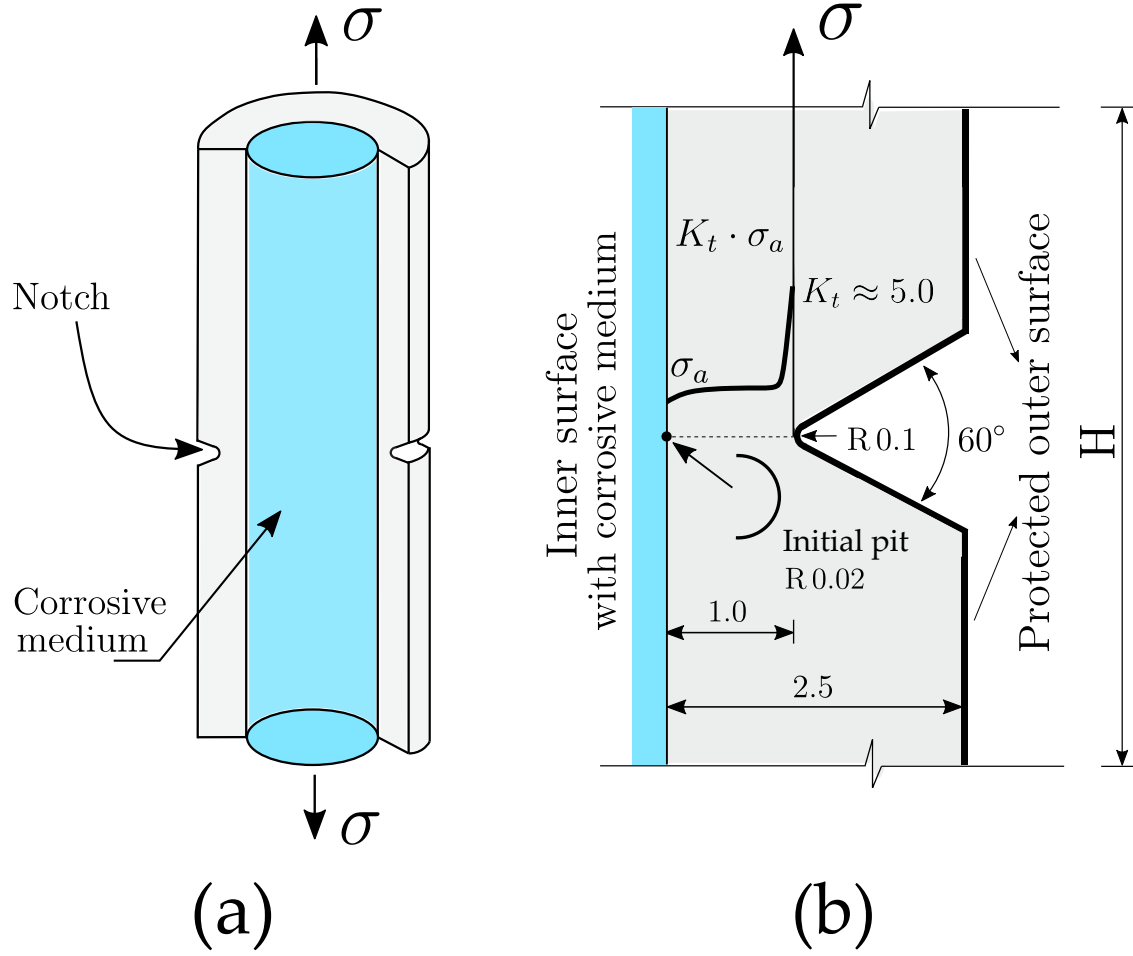


Figure 16: Gruhl (1984) experiments: (a) Testing configuration, and (b) detailed view of the geometry, with dimensions given in mm. Anodic-driven damage mechanisms should trigger cracks in the surface in contact with the environment, while cracking due to hydrogen embrittlement will be favoured near the notch region, where hydrogen accumulates due to higher hydrostatic stresses.

More specifically, Gruhl (1984) conducted experiments on AlZn5Mg3 using an aqueous solution containing 2% NaCl and 0.5% Na2CrO4 , with the pH value being adjusted to equal 3 (i.e., corrosion regime). The samples were hollow cylinders with the dimensions shown in Fig. 16, and had outer notches of 1.5 mm depth and 0.1 mm tip radius. Only the inner surface of the samples was exposed to the environment, while the outer surface was protected against air humidity. After some time of exposure, a constant tensile load was applied and held fixed until cracking was observed. The fracture surfaces were then carefully examined and the locations of crack initiation and propagation were identified. This ingenious testing protocol showed that brittle cracking occurred, with cracks initiating from the outer surface, near the notch tip and far away from the corrosive environment. Since hydrogen diffuses through the crystal lattice

and accumulates near stress concentrators such as notches or cracks, these findings revealed the important role of hydrogen embrittlement in the SCC of Al alloys.

Mimicking the experiments by Gruhl (1984) (see also Ratke and Gruhl, 1980), we model a cylindrical specimen subjected to constant uniaxial stress with the dimensions given in Fig. 16b. The experimental specimens have five identical surface notches, each separated by a distance of 30 mm. We find through preliminary simulations that the notch interaction effects are negligible and thus choose to simulate a single notch in a region of $H = 30$ mm height. In terms of material properties, the mechanical behaviour of the heat treated AlZn5Mg3 is characterised by a Young's modulus of $E = 71.7$ GPa, a Poisson's ratio of $\nu = 0.33$, a yield strength of $\sigma_y = 550$ MPa, and a strain hardening exponent of $N = 0.2$ (Diego Fuentes et al., 2018). From the fracture toughness measurements by Diego Fuentes et al. (2018), the critical energy release rate in an inert environment is estimated to be $G_c(0) = 8.5$ kJ/m². The hydrogen diffusion coefficient is taken to be $D_H = 9.3 \times 10^{-6}$ mm²/s, as reported by Young and Scully (2002). Gruhl (1984) and Ratke and Gruhl (1980) found that cracking was of intergranular nature, and thus we consider a grain boundary trap binding energy in (30). Specifically, a value of $\Delta g_b^0 = 19.3$ kJ/mol is adopted (see Su et al., 2019). The hydrogen damage coefficient is taken to be equal to $\chi = 0.67$, as estimated for Al alloys in the first principles calculations conducted by Jiang and Carter (2004). Regarding the electrochemical parameters, we follow Nguyen et al. (2018) and assume a metal ion diffusion coefficient of $D_M = 5.41 \times 10^{-4}$ mm²/s, an interface energy of $\gamma = 120$ J/m², a free energy density curvature of $A = 733$ N/mm², and a normalised saturated concentration of $c_{Le} = 0.03$. The interface thickness in this case study is chosen to be $\ell_d = 0.03$ mm, and the interface kinetics coefficient is initially defined as $L_0 = 1 \times 10^{-9}$ mm²/(N · s), but this magnitude is varied to investigate its influence. The fracture length scale parameter is defined to be $\ell_f = 0.1$ mm, as estimated from (60) and a tensile strength of $\sigma_c = 825$ MPa. Also, we adopt $\beta_e = 1$ and $\beta_p = 0.1$ in (66). As in the experiments, the sample is subjected to a constant load, resulting in a remote applied stress of $\sigma_a = 200$ MPa, which is applied after 24 hours of exposure to the corrosive environment. In our model, the vertical displacements are constrained so as to obtain an average remote stress of 200 MPa. Taking advantage of symmetry, we employ axisymmetric finite elements and accordingly modify the strain-displacement matrix. Also, only half of the 2D section is simulated, with appropriate symmetry boundary conditions along the

symmetry line. The finite element mesh is refined in the expected pitting and SCC regions; after a sensitivity study, we employ approximately 20,000 quadratic quadrilateral elements with reduced integration. We emphasise that the outer surface is protected and not exposed to an aggressive environment and thus the penalty condition $c_H = c_{\text{env}}$ is only defined at the inner surface.

First, simulations are conducted in the absence of corrosion or damage (i.e., $\phi_d = \phi_f = 1 \forall \mathbf{x}$) to gain insight into the diffusion of hydrogen within the sample. The experimental protocol involved an initial charging time (with no load) followed by a period combining environmental exposure and application of a constant tensile stress. For a stress of 200 MPa, failure was found to occur after 11 h, with cracks initiating solely near the tip of the notch. It was thus speculated that SCC cracking in AlZn5Mg3 was the result of the transport of hydrogen from the corrosive medium to the vicinity of the notch. The results obtained in this work in terms of stress and hydrogen distribution appear to strengthen that hypothesis. As shown in Fig. 17, hydrogen starts accumulating near the notch tip, at a distance from the inner surface that coincides with the peak stress, reaching a magnitude comparable to that of the inner surface after 11 h of loading time. Thus, it appears sensible to deduce that a critical combination of stress and hydrogen content has been achieved after 11 h, which has led to hydrogen-driven SCC from the notch tip. It should be noted that the consideration of plastic strain gradients would have displaced the stress and hydrogen peaks even closer to the notch tip (see Martínez-Pañeda et al., 2017).

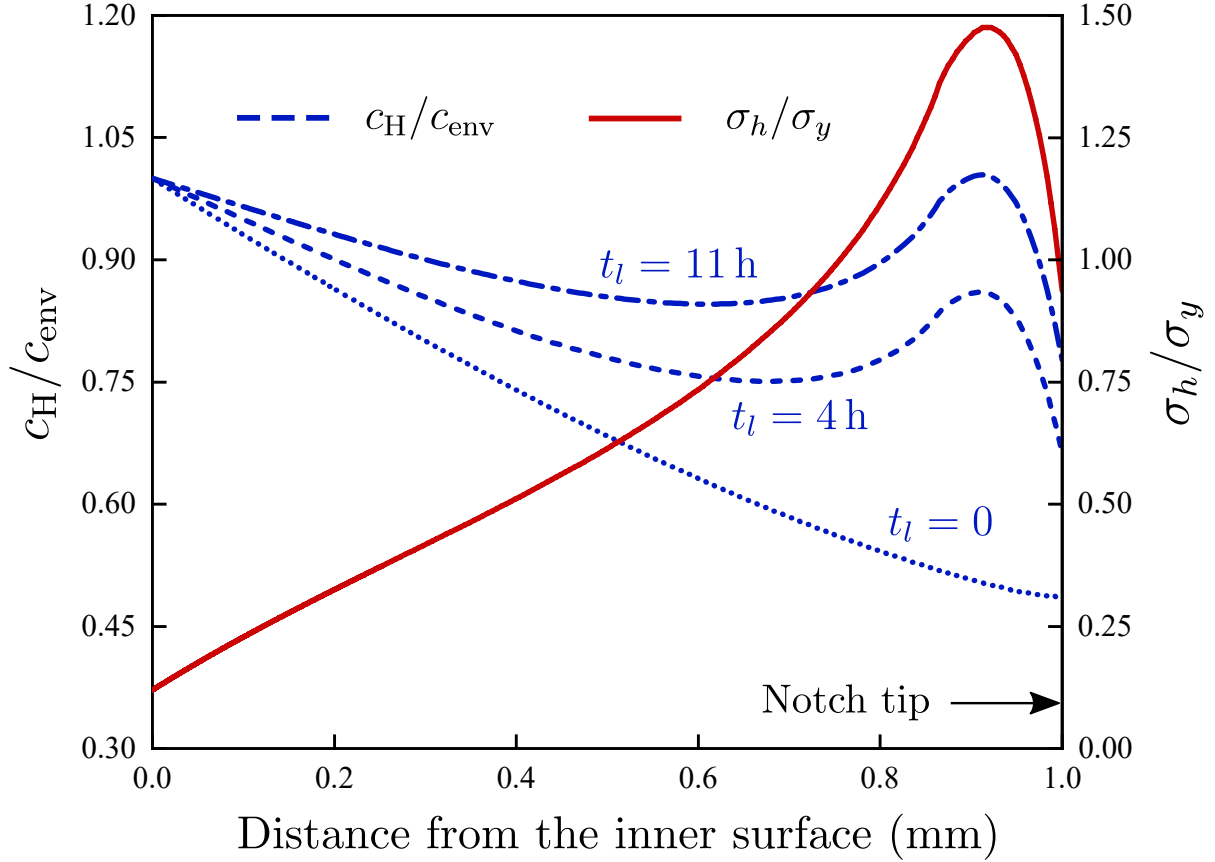


Figure 17: Gruhl (1984) experiments: normalised hydrogen concentration and hydrostatic stress distributions along the sample in the absence of phase field corrosion and damage ($\phi_d = \phi_f = 1 \forall \mathbf{x}$). Here, t_l denotes the time that has passed since a constant load is applied (i.e., after a pre-exposure time of 24 h).

We proceed to gain further insight by explicitly simulating the corrosion and cracking processes. To this end, a small pit of radius $R = 0.02$ mm is introduced in the inner surface to trigger anodic dissolution. The magnitude of c_{env} was not reported and can range from tens to hundreds of parts per million in weight (Scully et al., 2012). A value of $c_{\text{env}} = 72$ wppm is adopted, as this leads to a good approximation to the failure times reported by Gruhl (1984). As shown at the left edge of Fig. 18, a good agreement is attained with the experimental reported failure times for these assumptions. As can be observed in the embedded contours, failure is driven by hydrogen damage, with cracks nucleating close to the tip of the notch and propagating towards the inner sample surface.

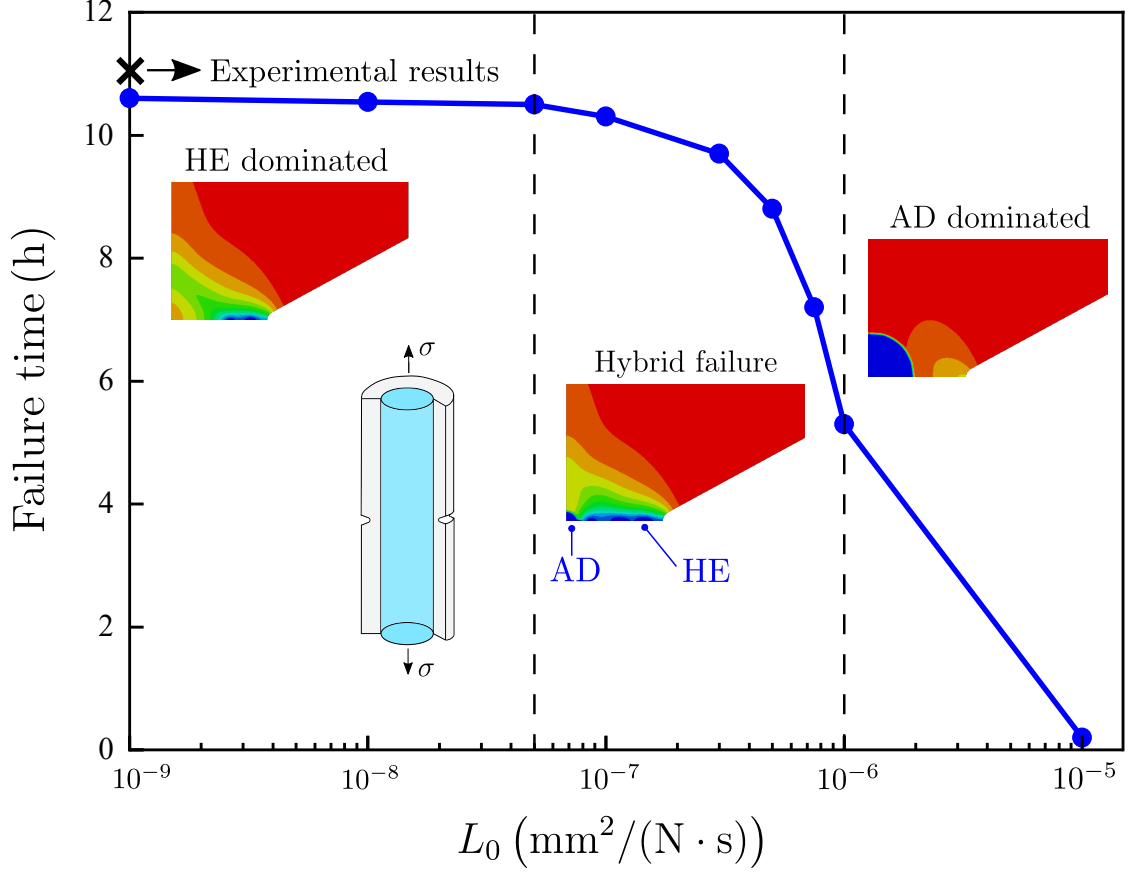


Figure 18: Gruhl (1984) experiments: failure time versus interface kinetics coefficient L_0 . Phase field ϕ_e contours are embedded to showcase the competing failure mechanisms and their dependence of L_0 . Increasing L_0 is associated with higher corrosion current densities and thus a transition is observed between hydrogen embrittlement, hybrid anodic dissolution and hydrogen embrittlement, and anodic dissolution.

Then, the interface mobility coefficient L_0 is varied to investigate the dependency of the failure mechanism on the environment. As elaborated in Section 4.4, L_0 is proportional to the corrosion current density i and thus increasing its value allows us to investigate more aggressive corrosive environments. As shown in Fig. 18, increasing L_0 leads to a shift in the failure mechanism and a drop in the failure time. Initially, the failure time appears to be insensitive to L_0 , as failure is purely driven by hydrogen embrittlement and as result the failure time is governed by the diffusion process; 10.6 h are needed for enough hydrogen to accumulate at the tip of the notch. However, as L_0 increases beyond 10^{-7} mm²/(N·s), pitting is observed to occur, which lowers the overall stiffness of the sample and triggers earlier failures. In this regime, the failure mechanism is a combination of hydrogen embrittlement and anodic dissolution as pitting initiates first but the main crack extends from the notch pit. Dissolution becomes dominant for

L_0 values larger than 10^{-6} mm²/(N·s), where pitting corrosion becomes significant even during the pre-charging time, leading to an almost sudden drop in the load carrying capacity upon the application of a remote displacement. The results shown in Fig. 18 illustrate the competition between the kinetics of anodic- and hydrogen-driven failure mechanisms, and extend the seminal experiments by Gruhl (1984) into regimes of higher corrosion currents, where anodic dissolution could have played a dominant role.

5. Discussion and summary

We have presented a generalised theory for stress corrosion cracking (SCC), incorporating both hydrogen embrittlement and material dissolution-driven damage mechanisms. The main ingredients of our formulation are: (i) a Cahn-Hilliard type evolution law for the mass-conserved diffusion of metal ions in the aqueous electrolyte; (ii) a KKS-based phase field model for describing material dissolution; (iii) an extended version of Fick’s law to characterise the diffusion of hydrogen atoms within the metallic lattice; (iv) a power-law elastic-plastic constitutive material model; and (v) a Griffith-based phase field description of the solid-crack interface. These elements are strongly coupled to capture key phenomena such as the interplay between diffusion and activation controlled corrosion, the role of film rupture and repassivation, the enhancement of corrosion kinetics due to mechanical contributions, the accumulation of hydrogen in areas of high volumetric strains, the sensitivity of material toughness to hydrogen content, and the synergy of multiple mechanisms in driving material degradation.

A numerical framework was also presented, which takes as degrees-of-freedom the displacement components, the phase field corrosion order parameter, the normalised concentration of metallic ions, the hydrogen concentration, and the phase field fracture order parameter. The resulting finite element model was used to conduct numerical experiments of particular relevance. First, the model was verified by reproducing two paradigmatic benchmarks in, respectively, corrosion and hydrogen embrittlement; the growth of a semi-circular pit and the failure of a notched square plate exposed to a hydrogen-containing environment. Then, insight was gained into the interaction and competition between the kinetics and damage mechanisms of hydrogen embrittlement and anodic dissolution. Firstly, SCC under pure bending in stainless steel was investigated, showcasing the important role of film passivation in preventing hydrogen uptake

and in governing the transition from anodic dissolution driven SCC growth to hydrogen assisted fracture. Secondly, the threshold stress intensity factor for SCC was quantified for a wide range of applied potentials and two different environments: sterile and biologically active seawater. The results showed a very good agreement with experiments and showcased the capability of the model in capturing the change in damage mechanism observed when the applied potential is varied. Finally, we have provided the first simulation results for the experiments by Gruhl (1984) on Al alloys. The finite element results obtained provide a mechanistic interpretation of these seminal experiments and extend the findings to more aggressive corrosive environments, quantifying the threshold at which hydrogen embrittlement ceases to dominate SCC in Al alloys. Through these numerical experiments, new physical insight is gained. In particular, it is worth emphasising and discussing the following findings:

- The interplay between mechanics and material dissolution accelerates the localisation of corrosion. As pits and other SCC defects become sharper, this leads to a localised rupture of the passive film and higher dissolution rates due to higher local mechanical fields (σ_h , ε^p).
- Defects that initially grow due to localised anodic dissolution can be driven by hydrogen embrittlement mechanisms at later stages, due to the increased accumulation of hydrogen with time and the rise in hydrostatic stress (and thus hydrogen content) that results for the sharpening of the SCC defect.
- The drop in toughness observed for applied potentials larger than the corrosion potential can be both due to increasing dissolution rates with E_p or due to the larger generation of hydrogen at the crack faces (or a combination of both).
- While hydrogen degradation laws based on first principles are appealing, as they require no calibration, fully predictive estimations are hindered by the uncertainties associated with the estimation of trap binding energies. On the other hand, quantitative estimates of material dissolution can be attained based on the corrosion current density.
- Film repassivation and hydrogen exhibit a complex interplay. A more stable film results in a reduced hydrogen uptake but also requires failure loads of higher magnitude, which favour a transition from anodic dissolution to hydrogen embrittlement.

The model presented not only enables investigating the interplay between hydrogen and anodic dissolution-driven damage mechanisms but also provides a generalised platform for predicting SCC across for arbitrary choices of material, loading conditions and environment.

Acknowledgements

C. Cui acknowledges valuable discussions with Dr Z. Cui and Dr H. Tian from the Ocean University of China. C. Cui and R. Ma acknowledge financial support from the National Natural Science Foundation of China (grants 52178153 and 51878493). E. Martínez-Pañeda acknowledges financial support from the EPSRC [grant EP/V009680/1] and from UKRI's Future Leaders Fellowship programme [grant MR/V024124/1]. C. Cui additionally acknowledges financial support from the China Scholarship Council (grant 202006260917).

References

- Abubakar, A.A., Akhtar, S.S., Arif, A.F.M., 2015. Phase field modeling of V2O5 hot corrosion kinetics in thermal barrier coatings. *Computational Materials Science* 99, 105–116.
- Alvaro, A., Thue Jensen, I., Kheradmand, N., Løvvik, O.M., Olden, V., 2015. Hydrogen embrittlement in nickel, visited by first principles modeling, cohesive zone simulation and nanomechanical testing. *International Journal of Hydrogen Energy* 40, 16892–16900.
- Amor, H., Marigo, J.J., Maurini, C., 2009. Regularized formulation of the variational brittle fracture with unilateral contact: Numerical experiments. *Journal of the Mechanics and Physics of Solids* 57, 1209–1229.
- Anand, L., Mao, Y., Talamini, B., 2019. On modeling fracture of ferritic steels due to hydrogen embrittlement. *Journal of the Mechanics and Physics of Solids* 122, 280–314.
- Andresen, P.L., Ford, F.P., 1988. Life prediction by mechanistic modeling and system monitoring of environmental cracking of iron and nickel alloys in aqueous systems. *Materials Science and Engineering* 103, 167–184.
- Ansari, T.Q., Huang, H., Shi, S.Q., 2021. Phase field modeling for the morphological and microstructural evolution of metallic materials under environmental attack. *npj Computational Materials* 7, 143.

- Asaoka, T., Dagbert, C., Aucoeur, M., Galland, J., 1977. Quantitative study of trapping characteristics of H in a Fe-0.15Ti ferrite by high-resolution autoradiography and during regassing at high temperatures. *Scripta Materialia* 11, 467–472.
- Barrera, O., Bombac, D., Chen, Y., Daff, T.D., Galindo-Nava, E., Gong, P., Haley, D., Horton, R., Katzarov, I., Kermode, J.R., Liverani, C., Stopher, M., Sweeney, F., 2018. Understanding and mitigating hydrogen embrittlement of steels: a review of experimental, modelling and design progress from atomistic to continuum. *Journal of Materials Science* 53, 6251–6290.
- Billingham, J., Sharp, J.V., Spurrier, J., Kilgallon, P.J., 2003. Review of the performance of high strength steels used offshore. Technical Report. Cranfield University.
- Borden, M.J., Hughes, T.J.R., Landis, C.M., Anvari, A., Lee, I.J., 2016. A phase-field formulation for fracture in ductile materials: Finite deformation balance law derivation, plastic degradation, and stress triaxiality effects. *Computer Methods in Applied Mechanics and Engineering* 312, 130–166.
- Bourdin, B., Francfort, G.A., Marigo, J.J., 2008. The variational approach to fracture. Springer Netherlands.
- Castelluccio, G.M., Geller, C.B., McDowell, D.L., 2018. A rationale for modeling hydrogen effects on plastic deformation across scales in FCC metals. *International Journal of Plasticity* 111, 72–84.
- Chen, J., Young, B., 2006. Stress-strain curves for stainless steel at elevated temperatures. *Engineering Structures* 28, 229–239.
- Chen, Z., Jafarzadeh, S., Zhao, J., Bobaru, F., 2021. A coupled mechano-chemical peridynamic model for pit-to-crack transition in stress corrosion cracking. *Journal of the Mechanics and Physics of Solids* 146, 104203.
- Choo, W.Y., Lee, J.Y., 1982. Thermal Analysis of Trapped Hydrogen in Pure Iron. *Metallurgical Transactions A* 13, 423–427.
- Cui, C., Ma, R., Martínez-Pañeda, E., 2021. A phase field formulation for dissolution-driven stress corrosion cracking. *Journal of the Mechanics and Physics of Solids* 147, 104254.

- Dekker, R., van der Meer, F.P., Maljaars, J., Sluys, L.J., 2021. A level set model for stress-dependent corrosion pit propagation. *International Journal for Numerical Methods in Engineering* 122, 2057–2074.
- Diego Fuentes, J., Cicero, S., Berto, F., Torabi, A.R., Madrazo, V., Azizi, P., 2018. Estimation of fracture loads in AL7075-T651 notched specimens using the equivalent material concept combined with the strain energy density criterion and with the theory of critical distances. *Metals* 8.
- Djukic, M.B., Bakic, G.M., Sijacki Zeravcic, V., Sedmak, A., Rajicic, B., 2019. The synergistic action and interplay of hydrogen embrittlement mechanisms in steels and iron: Localized plasticity and decohesion. *Engineering Fracture Mechanics* 216, 106528.
- Duda, F.P., Ciarbonetti, A., Sánchez, P.J., Huespe, A.E., 2015. A phase-field/gradient damage model for brittle fracture in elastic-plastic solids. *International Journal of Plasticity* 65, 269–296.
- Duda, F.P., Ciarbonetti, A., Toro, S., Huespe, A.E., 2018. A phase-field model for solute-assisted brittle fracture in elastic-plastic solids. *International Journal of Plasticity* 102, 16–40.
- Duddu, R., 2014. Numerical modeling of corrosion pit propagation using the combined extended finite element and level set method. *Computational Mechanics* 54, 613–627.
- Duddu, R., Kota, N., Qidwai, S.M., 2016. An Extended Finite Element Method Based Approach for Modeling Crevice and Pitting Corrosion. *Journal of Applied Mechanics* 83, 1–10.
- Engelhardt, G.R., Macdonald, D.D., Urquidi-Macdonald, M., 1999. Development of fast algorithms for estimating stress corrosion crack growth rate. volume 41.
- Ernst, P., Newman, R.C., 2002. Pit growth studies in stainless steel foils. I. Introduction and pit growth kinetics. *Corrosion Science* 44, 927–941.
- Ford, F., 1990. The Crack-Tip System and Its Relevance to the Prediction of Cracking in Aqueous Environments. *Environment Induced Cracking of Metals* , 139–166.
- Galvele, J.R., 1987. A stress corrosion cracking mechanism based on surface mobility. *Corrosion Science* 27, 1–33.

- Gangloff, R.P., 2003. Hydrogen-assisted Cracking, in: Milne, I., Ritchie, R., Karihaloo, B. (Eds.), *Comprehensive Structural Integrity Vol. 6*. Elsevier Science, New York, NY, pp. 31–101.
- Gao, H., Ju, L., Duddu, R., Li, H., 2020. An efficient second-order linear scheme for the phase field model of corrosive dissolution. *Journal of Computational and Applied Mathematics* 367, 112472.
- Gerberich, W.W., Oriani, R.A., Lii, M., Chen, X., Foecke, T., 1991. The necessity of both plasticity and brittleness in the fracture thresholds of iron. *Philosophical Magazine A* 63, 363–376.
- Gruhl, W., 1984. Stress Corrosion Cracking of High Strength Aluminium Alloys. *Zeitschrift fuer Metallkunde* 75, 819–826.
- Gurtin, M.E., Fried, E., Anand, L., 2010. *The Mechanics and Thermodynamics of continua*. Cambridge University Press, Cambridge, UK.
- Gutman, E.M., 1998. *Mechanochemistry of materials*. Cambridge International Science Publishing, Cambridge, UK.
- Gutman, E.M., 2007. An inconsistency in "film rupture model" of stress corrosion cracking. *Corrosion Science* 49, 2289–2302.
- Harris, Z.D., Lawrence, S.K., Medlin, D.L., Guetard, G., Burns, J.T., Somerday, B.P., 2018. Elucidating the contribution of mobile hydrogen-deformation interactions to hydrogen-induced intergranular cracking in polycrystalline nickel. *Acta Materialia* 158, 180–192.
- Hirth, J.P., 1980. Effects of hydrogen on the properties of iron and steel. *Metallurgical Transactions A* 11, 861–890.
- Isfandbod, M., Martínez-Pañeda, E., 2021. A mechanism-based multi-trap phase field model for hydrogen assisted fracture. *International Journal of Plasticity* 144, 103044.
- Jiang, D.E., Carter, E.A., 2004. First principles assessment of ideal fracture energies of materials with mobile impurities: Implications for hydrogen embrittlement of metals. *Acta Materialia* 52, 4801–4807.

- Jivkov, A.P., 2004. Strain-induced passivity breakdown in corrosion crack initiation. *Theoretical and Applied Fracture Mechanics* 42, 43–52.
- Kim, S.G., Kim, W.T., Suzuki, T., 1999. Phase-field model for binary alloys. *Physical Review E - Statistical Physics, Plasmas, Fluids, and Related Interdisciplinary Topics* 60, 7186–7197.
- Komaragiri, U., Agnew, S.R., Gangloff, R.P., Begley, M.R., 2008. The role of macroscopic hardening and individual length-scales on crack tip stress elevation from phenomenological strain gradient plasticity. *Journal of the Mechanics and Physics of Solids* 56, 3527–3540.
- Kristensen, P.K., Niordson, C.F., Martínez-Pañeda, E., 2020a. A phase field model for elastic-gradient-plastic solids undergoing hydrogen embrittlement. *Journal of the Mechanics and Physics of Solids* 143, 104093.
- Kristensen, P.K., Niordson, C.F., Martínez-Pañeda, E., 2020b. Applications of phase field fracture in modelling hydrogen assisted failures. *Theoretical and Applied Fracture Mechanics* 110, 102837.
- Kristensen, P.K., Niordson, C.F., Martínez-Pañeda, E., 2021. An assessment of phase field fracture: crack initiation and growth. *Philosophical Transactions of the Royal Society A: Mathematical, Physical and Engineering Sciences* 379, 20210021.
- Kumar, R., Mahajan, D.K., 2020. Hydrogen distribution in metallic polycrystals with deformation. *Journal of the Mechanics and Physics of Solids* 135, 103776.
- Lee, Y., Gangloff, R.P., 2007. Measurement and modeling of hydrogen environment-assisted cracking of ultra-high-strength steel. *Metallurgical and Materials Transactions A: Physical Metallurgy and Materials Science* 38 A, 2174–2190.
- Lin, C., Ruan, H., 2021. Phase-Field Modeling of Mechano–chemical-coupled Stress-Corrosion Cracking. *Electrochimica Acta* , 139196.
- Lufrano, J., Sofronis, P., Birnbaum, H.K., 1998. Elastoplastically accommodated hydride formation and embrittlement. *Journal of the Mechanics and Physics of Solids* 46, 1497–1520.

- Luo, Y., Li, W., Jiang, L., Zhong, N., Jin, X., 2021. Hydrogen embrittlement and hydrogen diffusion behavior in interstitial nitrogen-alloyed austenitic steel. *International Journal of Hydrogen Energy* 46, 32710–32722.
- Lynch, S., 2019. Discussion of some recent literature on hydrogen-embrittlement mechanisms: Addressing common misunderstandings. *Corrosion Reviews* 37, 377–395.
- MacDonald, D.D., Urquidi-MacDonald, M., 1991. A coupled environment model for stress corrosion cracking in sensitized type 304 stainless steel in LWR environments. *Corrosion Science* 32, 51–81.
- Mai, W., Soghrati, S., 2017. A phase field model for simulating the stress corrosion cracking initiated from pits. *Corrosion Science* 125, 87–98.
- Mai, W., Soghrati, S., Buchheit, R.G., 2016. A phase field model for simulating the pitting corrosion. *Corrosion Science* 110, 157–166.
- Mandal, T.K., Nguyen, V.P., Wu, J.Y., 2021. Comparative study of phase-field damage models for hydrogen assisted cracking. *Theoretical and Applied Fracture Mechanics* 111.
- Martínez-Pañeda, E., 2021. Progress and opportunities in modelling environmentally assisted cracking. *RILEM Technical Letters* 6, 70–77.
- Martínez-Pañeda, E., del Busto, S., Betegón, C., 2017. Non-local plasticity effects on notch fracture mechanics. *Theoretical and Applied Fracture Mechanics* 92, 276–287.
- Martínez-Pañeda, E., del Busto, S., Niordson, C.F., Betegón, C., 2016a. Strain gradient plasticity modeling of hydrogen diffusion to the crack tip. *International Journal of Hydrogen Energy* 41, 10265–10274.
- Martínez-Pañeda, E., Deshpande, V.S., Niordson, C.F., Fleck, N.A., 2019. The role of plastic strain gradients in the crack growth resistance of metals. *Journal of the Mechanics and Physics of Solids* 126, 136–150.
- Martínez-Pañeda, E., Fleck, N.A., 2019. Mode I crack tip fields: Strain gradient plasticity theory versus J2 flow theory. *European Journal of Mechanics - A/Solids* 75, 381–388.

- Martínez-Pañeda, E., Golahmar, A., Niordson, C.F., 2018. A phase field formulation for hydrogen assisted cracking. *Computer Methods in Applied Mechanics and Engineering* 342, 742–761.
- Martínez-Pañeda, E., Harris, Z.D., Fuentes-Alonso, S., Scully, J.R., Burns, J.T., 2020. On the suitability of slow strain rate tensile testing for assessing hydrogen embrittlement susceptibility. *Corrosion Science* 163, 108291.
- Martínez-Pañeda, E., Niordson, C.F., Gangloff, R.P., 2016b. Strain gradient plasticity-based modeling of hydrogen environment assisted cracking. *Acta Materialia* 117, 321–332.
- Miehe, C., Hofacker, M., Welschinger, F., 2010. A phase field model for rate-independent crack propagation: Robust algorithmic implementation based on operator splits. *Computer Methods in Applied Mechanics and Engineering* 199, 2765–2778.
- Narayan, S., Anand, L., 2019. A gradient-damage theory for fracture of quasi-brittle materials. *Journal of the Mechanics and Physics of Solids* 129, 119–146.
- Nguyen, T.T., Bolivar, J., Shi, Y., Réthoré, J., King, A., Fregonese, M., Adrien, J., Buffiere, J.Y., Baietto, M.C., 2018. A phase field method for modeling anodic dissolution induced stress corrosion crack propagation. *Corrosion Science* 132, 146–160.
- Nguyen, T.T., Réthoré, J., Baietto, M.C., Bolivar, J., Fregonese, M., Bordas, S.P., 2017. Modeling of inter- and transgranular stress corrosion crack propagation in polycrystalline material by using phase field method. *Journal of the Mechanical Behavior of Materials* 26, 181–191.
- Papazafeiropoulos, G., Muñoz-Calvente, M., Martínez-Pañeda, E., 2017. Abaqus2Matlab: A suitable tool for finite element post-processing. *Advances in Engineering Software* 105, 9–16.
- Parkins, R.N., 1987. Factors Influencing Stress Corrosion Crack Growth Kinetics. *Corrosion* 43, 130–139.
- Parkins, R.N., 1996. Mechanistic Aspects of Intergranular Stress Corrosion Cracking of Ferritic Steels. *Corrosion* 52, 363–374.

- Pioszak, G.L., Gangloff, R.P., 2017. Hydrogen Environment Assisted Cracking of Modern Ultra-High Strength Martensitic Steels. *Metallurgical and Materials Transactions A: Physical Metallurgy and Materials Science* 48, 4025–4045.
- Raja, V.S., Shoji, T., 2011. Stress corrosion cracking: theory and practice. Woodhead Publishing Limited, Cambridge.
- Ratke, L., Gruhl, W., 1980. Model experiments concerning the mechanism of stress corrosion cracking of AlZnMg alloys. *Materials and Corrosion* 31, 768–773.
- Robinson, M.J., Kilgallon, P.J., 1994. Hydrogen Embrittlement of Cathodically Protected High-Strength, Low-Alloy Steels Exposed to Sulfate-Reducing Bacteria. *Corrosion* 50, 626–635.
- Schomberg, K., Grabke, H.J., 1996. Hydrogen permeation through oxide and passive films on iron. *Steel Research* 67, 565–572.
- Scully, J.C., 1975. Stress corrosion crack propagation: A constant charge criterion. *Corrosion Science* 15, 207–224.
- Scully, J.C., 1980. The interaction of strain-rate and repassivation rate in stress corrosion crack propagation. *Corrosion Science* 20, 997–1016.
- Scully, J.R., Young, G.A., Smith, S.W., 2012. Hydrogen embrittlement of aluminum and aluminum-based alloys, in: Gangloff, R.P., Somerday, P. (Eds.), *Gaseous Hydrogen Embrittlement of Materials in Energy Technologies Vol. I*. Woodhead Publishing, pp. 707–768.
- Serebrinsky, S., Carter, E.A., Ortiz, M., 2004. A quantum-mechanically informed continuum model of hydrogen embrittlement. *Journal of the Mechanics and Physics of Solids* 52, 2403–2430.
- Shishvan, S.S., Csányi, G., Deshpande, V.S., 2020. Hydrogen induced fast-fracture. *Journal of the Mechanics and Physics of Solids* 134, 103740.
- Sieradzki, K., Newman, R.C., 1985. Brittle behavior of ductile metals during stress-corrosion cracking. *Philosophical Magazine A: Physics of Condensed Matter, Structure, Defects and Mechanical Properties* 51, 95–132.

- Sofronis, P., Birnbaum, H., 1995. Mechanics of the hydrogen-dislocation-impurity interactions—I. Increasing shear modulus. *Journal of the Mechanics and Physics of Solids* 43, 49–90.
- Sofronis, P., McMeeking, R.M., 1989. Numerical analysis of hydrogen transport near a blunting crack tip. *Journal of the Mechanics and Physics of Solids* 37, 317–350.
- Su, H., Toda, H., Shimizu, K., Uesugi, K., Takeuchi, A., Watanabe, Y., 2019. Assessment of hydrogen embrittlement via image-based techniques in Al–Zn–Mg–Cu aluminum alloys. *Acta Materialia* 176, 96–108.
- Tanné, E., Li, T., Bourdin, B., Marigo, J.J., Maurini, C., 2018. Crack nucleation in variational phase-field models of brittle fracture. *Journal of the Mechanics and Physics of Solids* 110, 80–99.
- Tian, H., Wang, X., Cui, Z., Lu, Q., Wang, L., Lei, L., Li, Y., Zhang, D., 2018. Electrochemical corrosion, hydrogen permeation and stress corrosion cracking behavior of E690 steel in thiosulfate-containing artificial seawater. *Corrosion Science* 144, 145–162.
- Tondro, A., Abdolvand, H., 2021. Quantifying hydrogen concentration in the vicinity of zirconium hydrides and deformation twins. *Journal of the Mechanics and Physics of Solids* 148, 104287.
- Turnbull, A., 1993. Modelling of environment assisted cracking. *Corrosion Science* 34, 921–960.
- Turnbull, A., 2001. Modeling of the chemistry and electrochemistry in cracks - A review. *Corrosion* 57, 175–188.
- Williams, M.L., 1957. On the stress distribution at the base of a stationary crack. *Journal of Applied Mechanics* 24, 109–114.
- Wu, J.Y., Mandal, T.K., Nguyen, V.P., 2020. A phase-field regularized cohesive zone model for hydrogen assisted cracking. *Computer Methods in Applied Mechanics and Engineering* 358, 112614.
- Young, G.A., Scully, J.R., 2002. Hydrogen production, absorption and transport during environment assisted cracking of an Al–Zn–Mg–(Cu) alloy in humid air, in: *Proceedings of the*

International Conference on Hydrogen Effects on Material Behaviour and Corrosion Deformation Interactions, pp. 893–907.